Novel plasmonic interaction and manipulation in 2D materials

Jiang, Jing

2019

Jiang, J. (2019). Novel plasmonic interaction and manipulation in 2D materials. Doctoral thesis, Nanyang Technological University, Singapore.

https://hdl.handle.net/10356/92429

https://doi.org/10.32657/10220/49455

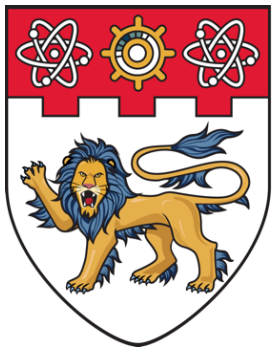

NANYANG TECHNOLOGICAL UNIVERSITY
SINGAPORE

NOVEL PLASMONIC INTERACTION AND MANIPULATION IN 2D MATERIALS

JING JIANG

SCHOOL OF PHYSICAL AND MATHEMATICAL SCIENCES

2019

NOVEL PLASMONIC INTERACTION AND MANIPULATION IN 2D MATERIALS

JING JIANG

SCHOOL OF PHYSICAL AND MATHEMATICAL SCIENCES

A thesis submitted to the Nanyang Technological University in partial fulfilment of the requirement for the degree of Doctor of Philosophy

2019

Statement of Originality

I hereby certify that the work embodied in this thesis is the result of original research done by me except where otherwise stated in this thesis. The thesis work has not been submitted for a degree or professional qualification to any other university or institution. I declare that this thesis is written by myself and is free of plagiarism and of sufficient grammatical clarity to be examined. I confirm that the investigations were conducted in accord with the ethics policies and integrity standards of Nanyang Technological University and that the research data are presented honestly and without prejudice.

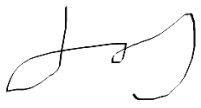

01/08/2019

. . . . . .
Date

. . . . . .
Jing Jiang

Supervisor Declaration Statement

I have reviewed the content and presentation style of this thesis and declare it of sufficient grammatical clarity to be examined. To the best of my knowledge, the thesis is free of plagiarism and the research and writing are those of the candidate's except as acknowledged in the Author Attribution Statement. I confirm that the investigations were conducted in accord with the ethics policies and integrity standards of Nanyang Technological University and that the research data are presented honestly and without prejudice.

01/10/2019

. . . . . .
Date

. . . . . .
Baile Zhang

Authorship Attribution Statement

This thesis contains material from 1 paper published in the following peer-reviewed journal where I was the first author.

Chapter 2.3, 2.4 is published as Jing Jiang, Daohua Zhang, Baile Zhang, and Yu Luo. Interaction between graphene-coated nanowires revisited with transformation optics. *Optics Letters* **42**, 2890-2893 (2017). DOI: 10.1364/OL.42.002890.

The contributions of the co-authors are as follows:

- I wrote the drafts of the manuscript. The manuscript was revised together with Prof Yu Luo, Prof Baile Zhang and Prof Daohua Zhang.
- Prof Yu Luo did the preliminary calculation on bare dimer structures in his previous work and the modified calculation for graphene-coated dimer is derived together with me.
- I developed the code to calculate the spectrum of the structure under study and the code is revised together with Prof Yu Luo.

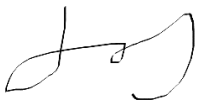

01/08/2019

. . . .

Date Jing Jiang

Abstract

Recently, ignited by the pioneer work in the area of graphene plasmonics, plasmonics with two dimensional (2D) materials which are atomically thin materials bonded by weak van der Waals interaction has gain considerable research interests. This thesis studies the novel interactions and manipulations of 2D plasmons which feature their exotic optical properties drastically different from their three-dimensional bulk counterparts, as well as the feasibility to be tuned through external modification such as chemical doping and electrical gating. In particular, we derive a full analytical solution of the optical response of a graphene-coated cylindrical dimer, and show a polarization independent broadband spectrum, as well as multi-frequency Fano dips, in contrast to its metallic counterparts. We further explore the negative fraction of extremely squeezed polaritons in nanostructured and natural hyperbolic 2D materials. At last, we demonstrate a directional waveguide design based on two inversely biased graphene sheets. The proposed work is significant in demonstrating 2D material as a versatile platform for nanophononics applications from several aspects and providing physical insight through comprehensive theoretical study.

Acknowledgements

First and foremost, I would like to express sincere gratitude to my supervisor Associate Professor Baile Zhang and co-supervisor Assistant Professor Yu Luo for their patient guidance, valuable advice and encouragement throughout the past four years of my postgraduate study. They set up a role model for me for their rigorous attitude towards theoretical electromagnetics study and day-to-day hard working in research. It's really my great honor and I feel very lucky to be student of Prof Zhang and Prof Luo who are excel in the research field of electromagnetics and are also very kind-hearted.

I'm particularly thankful to my senior colleague Dr. Xiao Lin for conceiving the insightful original ideas of the second and third projects of this thesis and conducting valuable discussions during the process that I implement the simulations and calculations. I'm always inspired by his enthusiasm and open mind for theoretical electromagnetics research.

I also would like to thank current and former group mates Dr. Hongyi Xu, Dr. Zhen Gao, Dr. Fei Gao, Dr. Xihang Shi, Dr. Youming Zhang, Dr. Zhaoju Yang, Dr. Hongli Chen, Dr. Yihao Yang, Haoran Xue, Yahui Yang, Guigeng Liu, Fuyang Tay, Dr. Liangliang Liu, Dr. Lin Wu, Yao Huang, Lin Liu, Hao Hu and Dongjue Liu for the fruitful discussions during weekly group meetings and the great time we had together in the past four years. Especially, I would like to thank Dr. Fei Gao for his valuable advice and suggestions as a senior and teach me a lot when we were attending PIERS conference at Russia. I would like to thank Dr. Youming Zhang and Dr. Xihang Shi for their help and discussions for problems I encountered in simulations and calculations.

Then I would like to thank Dr. Hongli Chen for her efforts on the attempts of microwave experiment collaborated with me where we faced the difficulties together.

Last but not the least, I would like to thank my family for their continued love and encouragement that let me never feel knocked down by difficulties in studies and life.

Table of Contents

List of figures

Figure.**4-4** Field pattern when double layer oppositely biased graphene sheets are excited by a linearly polarized point source.

Figure.**4-5** Unidirectional Y-shaped waveguide based on drift induced nonreciprocal graphene.

Chapter 1 Introduction

1.1 General properties of plasmon polaritons

Plasmon polaritons, which is defined as the coherent oscillations of conduction electrons at interface where the real part of the permittivity is opposite to the other side, has become an important subfield of nanophotonics.

The significance of the plasmon polariton is two-fold: firstly, the huge near-fields intensity and extreme charge accumulation leading to enhanced light-matter interactions, which is useful for single molecule biosensing applications and nonlinear phenomenon. Secondly, the highly squeezed surface plasmon down to the sub-wavelength level allows manipulation of light below the diffraction limit and therefore enables size reduction of optical components and high-resolution spectroscopy, which opens new avenues in the fields of photonics integrated circuitry and quantum information technology.

According to the type of interface plasmon is confined, it can be classified into surface plasmon polaritons (SPP) and localized plasmon polaritons (LSP). The former refers to propagating plasmon polaritons that are confined to a flat surface, such as metal-dielectric interface, while the later corresponds to non-propagating resonant plasmon modes confined at closed surfaces such as metallic nanoparticles.

1.1.1 Propagating surface plasmon polaritons (SPP)

SPPs are propagating electromagnetic waves coupled tightly to electron plasma at metal-dielectric interfaces. Subwavelength light confinement is achieved because of the evanescently decay electromagnetic wave on both sides of the interface (Fig.1-1 (b)). In this way, light is squeezed into nanoscale and thereby provide the basis for overcoming the usual diffraction limit that constrains the miniaturization and performance of photonic devices. Because the highly squeezed surface plasmon usually

has a wavevector much larger than that of the free space, dealing with the momentum mismatch is crucial for the excitation of SPPs. Common phase-matching methods adopted by researchers include prism [1], grating coupling [2,3] or via near-field optical microscopy technique [4]. Due to this strong spatial localization property, SPPs have become candidate of information carriers propagating in particularly designed plasmonic waveguides [5], laser [6], modulators [7] and switches [8], driven by the pursuit of photonic integrate circuitry and optical interconnection between photonics and electronic systems.

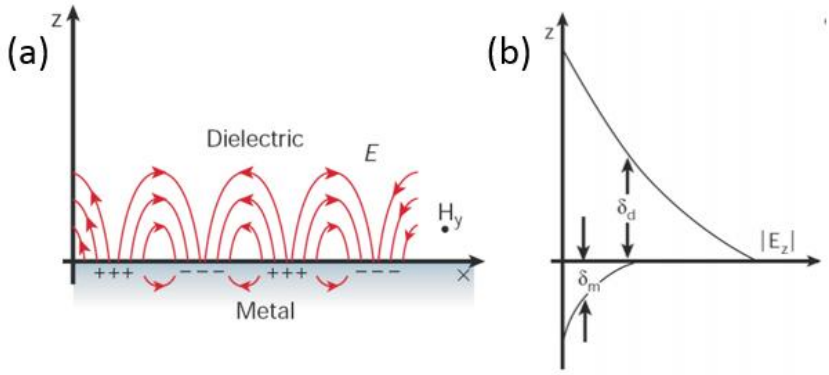

Figure.1-1 (a) Schematics of SPPs at the metal/dielectric interface. (b) evanescent fields normal to the interface [9].

1.1.2 Localized surface plasmon (LSP)

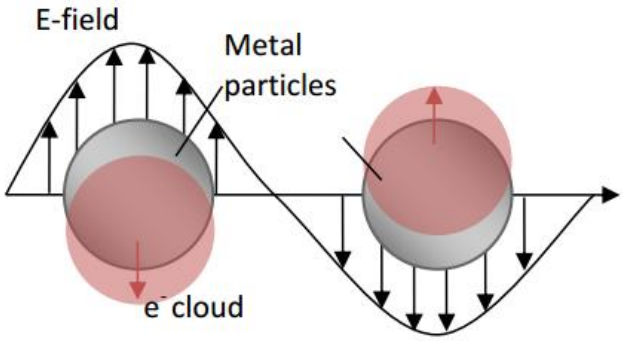

Figure.1-2 Schematic of LSP excited in a metal nanoparticle. The red shaded area illustrates the polarized electron cloud relative to the nuclei [10].

Localized surface plasmons are resonant modes of surface plasmon confined in conductive nanoparticles of sub-wavelength size, as illustrated in Fig.1-2. Under this

circumstance, the curved surface where electron gas is confined leads to an effective restoring force on the free conduction electrons, which give rise to particle-plasmon resonances, leading to strongly enhanced nearfield and charge accumulation inside the particle. The curved surface also enables excitation of LSP via direct light illumination, where the phase-matching process for SPP's excitation is no longer necessary. Before researchers establish concrete theory foundation and experimental verification of the LSP effect, it has been deployed by craftsman in ancient times in the staining of glass cups and church windows. Clear mathematical formulism was established in 1908 by Gustav Mie, by proposing the now widely used theory describing light scattering by spherical particles [11].

The properties of LSP modes depend strongly on the geometry, type of material of the nanostructure as well as the refractive index of the surrounding medium, making it suitable for sensing applications [12]. Furthermore, the enhanced near field around the nanoparticle is beneficial for light harvesting process such as photovoltaics [13,14], surface enhanced Raman scattering (SERS) [15] and fluorescence (SEF) [16], nonlinear optical effects [17], optical antennas [18] and light-matter interactions in quantum plasmonic systems [19].

The plasmon resonance has two competing damping channels, radiative damping due to direct decay of the coherent electron oscillation into photons [20] and non-radiative damping caused by absorption. According to different applications, it is always beneficial to tailor the plasmonic structures such that preferable damping process is made dominate while unwanted damping process is suppressed. For example, for applications such as SERS where sample heating or quenching of fluorescence from adsorbed molecules are to be avoided [21], nonradiative decay is unwanted and the radiative decay channel should dominate. While for sensing applications, the so-called

nonradiative “dark mode” resonance which cannot couple directly to the incident photon is preferred for its narrow line width which can improve the sensitivity. However, it is not possible to achieve these designs in individual particle with single metallic surface. Fortunately, advancement in nanofabrication technology and computational power have made it possible to realize complex plasmonic effects based on interference between multiple surfaces in core-shell particles, ensembles of nanoscale structures of various sizes and shapes such as dimer [22], dolmen structure [23] and ring-disk cavity [24].

For example, in Figure.1-3 (a) C. Argyropoulos et al. propose a core-shell particle structure with a silver shell and the core loaded with nonlinear Kerr material [17]. The abrupt switching between cloaks and resonant scatterers can be clearly observed from the normalized scattering cross-section (red solid line). The cloaking and scattering mode correspond to the dipolar bonding mode and the dipolar antibonding mode, respectively.

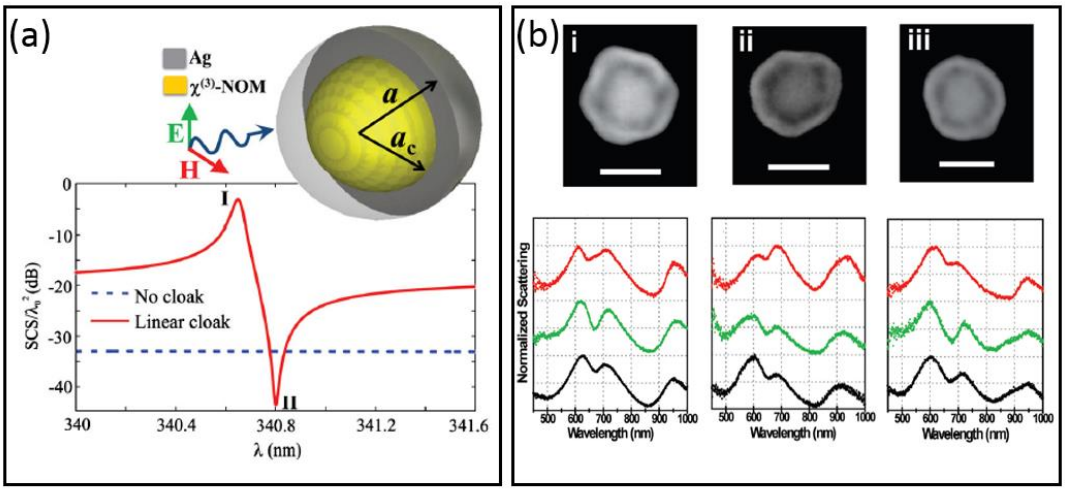

Figure.1-3 (a) Schematic of the core-shell particle and the normalized scattering cross-section against the wavelength [17]. (b) Upper panel: SEM image for three Au/SiO_2/Au nanoparticles. Lower panel: corresponding dark field scattering spectra for particles (i-iii), under different polarized incidence (unpolarized: black, s-polarized: green; p-

polarized: red) [25].

Interestingly, the author noticed that though the fields outside the dielectric core are drastically different for the resonant state and the cloaked state, but the fields inside the inner core is uniformly enhanced in both cases. Therefore, the nonlinear effects inside the core can be boosted based on this property. Similar effects also have been discussed in Ref. [25], as shown in Fig.1-3 (b), three Au/SiO_2/Au multilayer nanoparticles with distinct asymmetric geometry show different optical spectra (below the scanning electron microscopy (SEM) images), but all have two dips due to interference of the subradiant dipolar mode and the superradiant dipolar mode. These dips are known as plasmonic Fano resonances, which is the classical analogue of the typical spectral features induced by the coupling of a discrete state with a continuum first discovered in the field of atomic physics by Fano in 1961 [26].

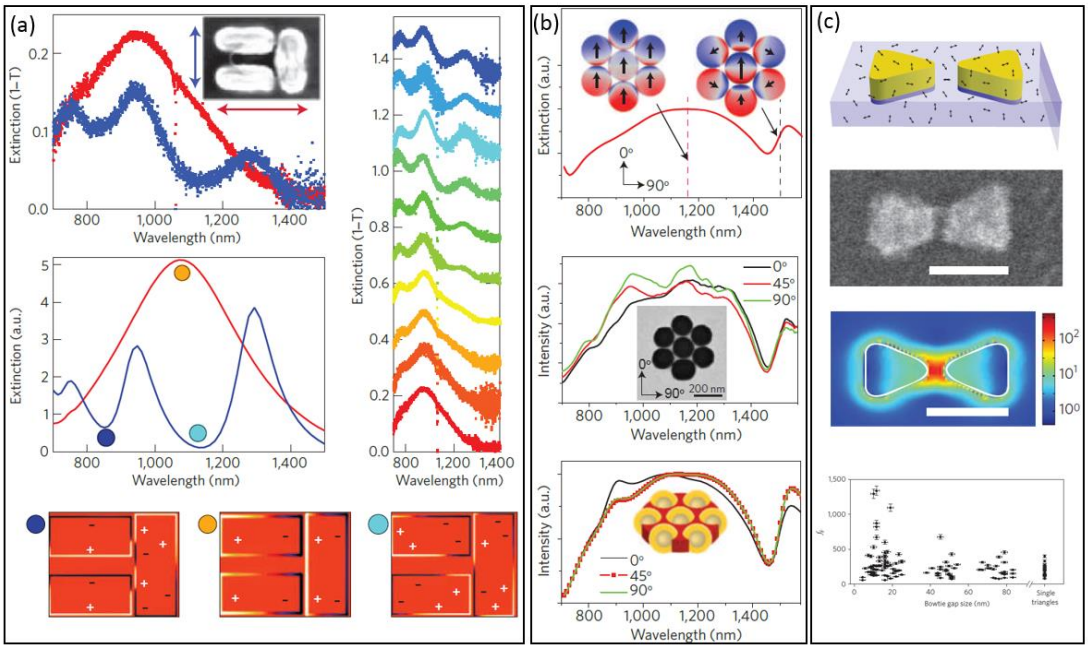

Figure.1-4 (a) Left panel: experimental (upper) and numerical simulated (lower) extinction spectrum of the dolmen structure. Blue and red line corresponds to polarizations along the red and blue arrows. Right panel: Evolution of the distinction spectra between two distinct polarization. Lower panel: charge distribution at the

extinction peak and dips [23]. (b) Upper to lower panel: Charge density plot, experimental and calculated spectra of a heptamer at different orientation angels [27]. (c) Upper to lower panel: schematics, SEM image, simulated fields distribution and fluorescence enhancement versus gap size of the bowtie nanoantenna [28].

Figure.1-4 shows three typical examples of ensembles of nanoscale structures where near-field coupling between individual structures is exploited to achieve complex plasmonic responses. As illustrated in Fig.1-4 (a) [23], for a dolmen structure made up of Au monomer and dimer, symmetry-breaking of the structure allows the nonradiative "dark" quadrupole (light blue dot) and bonding dipolar (dark blue dot) modes of the dimer to couple directly to the incident wave through hybridization with the "bright" dipole mode of the monomer, which can be inferred from the diagram of charge distribution in the lowest panel. Therefore, in the extinction spectra, multiple Fano dips can be observed (light and dark blue dots). Moreover, Ref. [27] demonstrates that Fano-like resonances can also be supported by self-assembled heptamer of metal spheres without the expenses of symmetry breaking, as shown in Fig.1-4 (b). Besides nanorods and spheres, in Ref. [28] gold bowtie nanoantenna is used to realize enhanced fluorescence up to a factor of 1340 for single molecule, taking advantage of the huge local intensity enhancement in the gap.

1.2 Plasmon polaritons in van der Waals materials

Recently, plasmonics with two dimensional (2D) or van der Waals (vdW) materials which are atomically thin materials bonded by weak vdW interaction has gain considerable research interests, especially after the pioneer work in the field of graphene plasmonics. The family of 2D materials spans a wide range, including metals, semimetals (graphene), semiconductors (black phosphorus, transition metal

dichalcogenides such as MoS2), and dielectrics (Boron Nitride). Optical properties of these 2D vdW materials are drastically different from their 3D bulk counterparts, leading to exotic phenomena that are useful for a variety of optoelectronic applications [29,30]. The in-plane conductivity for 2D vdW material can be written in the general form as [31]:

$$\sigma(\omega) = \frac{i}{\pi}\frac{S_{\mathrm{f}}}{\omega + i\tau_{\mathrm{f}}^{-1}} + \frac{i}{\pi}\frac{\omega S_{\mathrm{b}}}{\omega^2 - \omega_{\mathrm{b}}^2 + i\omega\tau_{\mathrm{b}}^{-1}} \tag{1.1}$$

Where S_{f} and S_{b} are the spectral weights of Drude and Lorentz terms representing the contribution of free and bound charges, respectively; ω_{b} is the exciton/phonon frequency; τ_{s} and τ_{b} are the phenomenological relaxation times. By active control of the spectral weights, polaritons in 2D vdW materials are often amenable to tuning through external modification such as chemical doping and electrical gating.

1.2.1 Graphene plasmonics

Metals commonly used in plasmonic structures suffers from severe ohmic loss in the frequency bands of interest which constitute a main hurdle to the wide application of these structures in optical devices. Therefore, researchers have been seeking for efficient loss compensation techniques and alternative materials that meet industrial demands for plasmonic systems. In this context, in the past decade graphene plasmonics have gained much research interests for its unique electro-optical properties. Compared to plasmons in noble metal, plasmon in graphene exhibits several features that made it superior:

Firstly, graphene has been theoretically and experimentally shown to support surface plasmon with high spatial confinement and relative low loss. Carriers in graphene behave like the so-called massless Dirac fermions, and the carrier mobility is extremely high (up to 200,000 $\mathrm{cm^2V^{-1}s^{-1}}$ [32]), even at room temperature. The

ultrahigh carrier mobility and the feature of ballistic transport lead into almost purely imaginary surface conductivity for graphene in the THz and infrared frequency range, which imply its low-loss and inductive properties. One of the important figures of merit characterize surface plasmon's level of confinement is the ratio of the plasmon wavevector to the free-space wavevector $\beta = \mathrm{Re}[q]/q_0$. Another important figure of merit is the inverse damping ratio $\gamma^{-1} = \mathrm{Re}[q]/\mathrm{Im}[q]$ while $\gamma^{-1}/2\pi$ describes the number of plasmon's maximum propagation cycle before the amplitude decays by $1/e$ [33]. A. Woessner et al. experimentally achieve $\beta \sim 150$, $\gamma^{-1} > 25$ and life time $\tau \sim 500$ fs in graphene encapsulated by hexagonal boron nitride (h-BN) [4], as shown in Figure.1-5 (a) and (b), where it can be clearly seen that graphene and other 2D vdW materials overperform the Au monolayer in terms of the confinement factor and damping ratio in the infrared regime. Furthermore, recently graphene-hBN heterostructure covered by metallic rod array is demonstrated to achieve ultimate plasmon confinement down to the scale of one atom, making use of the resonant modes of the metal rods [3].

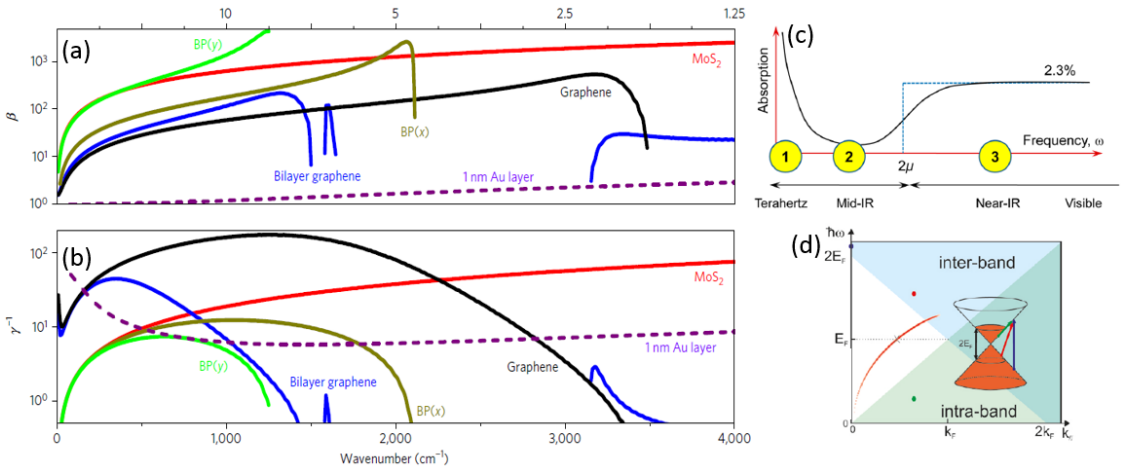

Figure.1-5 Calculated confinement factor β (a) and inverse damping ratio γ^{-1} (b) for Au monolayer, graphene and other 2D materials [33]. (c) Absorption spectrum of doped graphene [34]. (d) Dispersion diagram of surface plasmon mode for $E_F = 0.5$ eV, and the intra- and interband transitions in graphene [35].

Secondly, the carrier density which determines the weight of the Drude term (S_{f} in eq. (1.1)) can be continuous tuned by electrical gating [36], chemical doping [37] or optical pulses [38]. The imaginary part of the graphene surface conductivity can be largely tuned from negative to positive value depending on the chemical potential [39,40], leading to the alternation from dielectric to metallic behavior that result in graphene's semi-metallic nature, unlike noble metal in conventional plasmonics. As illustrated in Fig.1-5 (c) and (d), for higher frequency around near-infrared and visible region with $\hbar\omega > 2\mathrm{E_F}$ or 2μ, the graphene conductivity is dominated by the interband contribution, and has a universal value $\sigma_0 \approx e^2/4\hbar$, corresponding to a stable absorption of 2.3% which depends solely on the fine-structure constant [41]. On the other hand, for spectral weight below $2\mathrm{E_F}$, $\mathrm{Im}(\sigma)$ grows while $\mathrm{Re}(\sigma)$ decreases caused by Pauli blocking of the interband transitions, thus intraband transition of electrons plays an important role and make the Drude response dominate at the terahertz frequencies.

Advance in nano-fabrication and nano-imaging techniques empowered the fabrication, launching and visualizing of graphene plasmons. Scattering-type scanning near-field optical microscopy (SNOM) has been used in several experimental demonstrations for excitation and imaging of propagating plasmon polariton in graphene [4,42,43], where an atomic force microscope tip is used to mediate the phase-mismatch between free space light and confined graphene plasmons. As for fabrication techniques, besides the conventional mechanical exfoliation method, the standardized process of the growth of large-area graphene by chemical vapor deposition (CVD) [44] makes it possible to fabricate large-area samples which allows surface plasmon lifetimes reaching hundreds of optical cycles, thereby overcome one of the main restrictions facing convention noble-metal plasmonics. Furthermore, the development

of plasma etching [36] and the standardization of the procedure for graphene transfer [45] over other plasmonic structures pave the way for tailoring the shape of graphene and the integration of graphene with conventional plasmonic systems for field enhancement or addition of extra control.

Based on the abovementioned understanding of the nature of graphene and technical advances, below we will briefly review some designs based on monolayer [46], bilayer graphene [47], patterned graphene [36,48] and hybrid device where graphene is integrated with other photonic structure such as waveguides [46], single [49-53] and ensemble of plasmonic nanoparticles [45,54,55], as well as other 2D vdW materials [56].

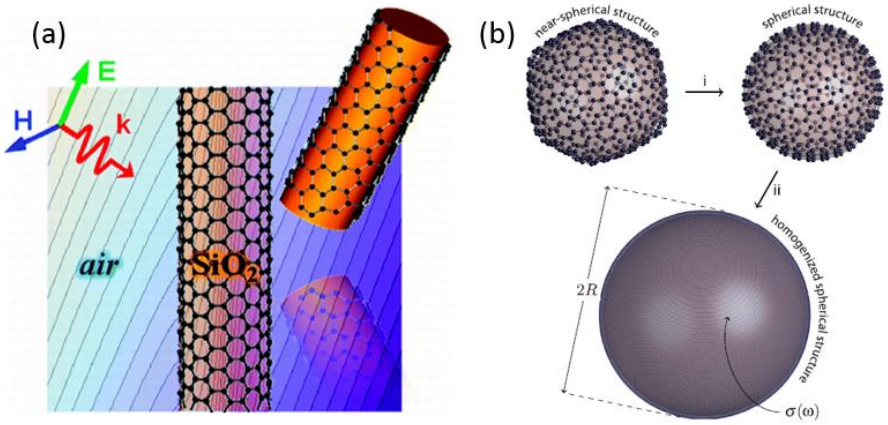

Figure.1-6 Schematic illustration of graphene coated (a) cylindrical [49] and (b) spherical [52] nanoparticles.

The integration of graphene with photonic structures is widely studied to bring about exceptional plasmonics effects. One of the simplest design one can think of is nanoparticles coated with graphene monolayer. Based on the scattering cancellation of the individual modes of the core and the shell, invisibility dips [49] and superscattering peaks [51] can be obtained in the spectra. Ref. [49] suggests that a tunable surface cloak can be achieved by wrapping a dielectric cylinder with graphene monolayer (Fig.1-6 (a)). In Ref. [52] the author theoretically studied the localized surface plasmon in a

graphene-coated spherical nanoparticle (Fig.1-6 (b)). Further studies on these graphene-coated spherical and cylindrical nanoparticles demonstrate that mode bifurcation and second-harmonic generation can be induced by the nonlinear conductivity of graphene [50,53].

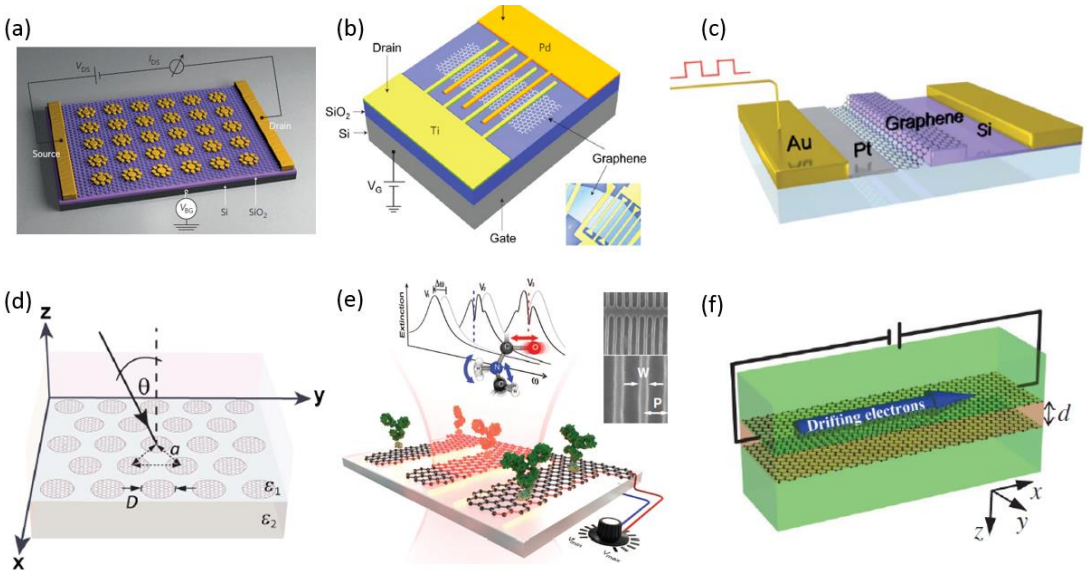

Figure.1-7 Schematics of (a) metallic nanoantenna-graphene phototransistor [55], (b) metal–graphene–metal photodetectors [57], (c) graphene-based optical modulator [46], (d) doped graphene nanodisks [48], (e) graphene biosensor [30] and (f) two graphene sheets separated by a Si gap [47].

The combination of graphene with conventional plasmonics helps to overcome the bottleneck of graphene's insufficient interaction with incident photon. For instance, LSP resonances with large near-field enhancement are utilized to enhance the light-matter interaction in graphene in Ref. [55] by placing metal nanoparticle near graphene (Fig.1-7 (a)). Also, in Ref. [57] the author report an asymmetric metal–graphene–metal photodetector with enhanced photoresponsivity under vertical incidence, where graphene is integrated with multiple interdigitated metal fingers for electric field enlargement (Fig.1-7 (b)). On the other hand, combination of graphene with conventional plasmonics provides extra control to the optical response, which is useful

for active plasmonic devices such as modulator [46] and sensor [30]. For example, Ming Liu et al. [46] experimentally demonstrate a broadband optical modulator based on combination of monolayer graphene with silicon waveguide, where the modulation is realized by tuning the Fermi level of graphene (Fig.1-7 (c)). Furthermore, altering the operating frequency from the optical to the THz and mid-infrared range is important for certain applications. For example, as shown in Fig.1-7 (e), sensors based on patterned graphene nanoribbon arrays show large sensitivity for biomolecule detection [30]. Besides graphene patterned into ribbon arrays, another design based on graphene nanodisk array is demonstrated to support 100% optical absorption [48]. Furthermore, in Ref. [47] the coupling between two graphene sheets is exploited to achieve plasmon amplification when the upper layer is biased with drifting electrons.

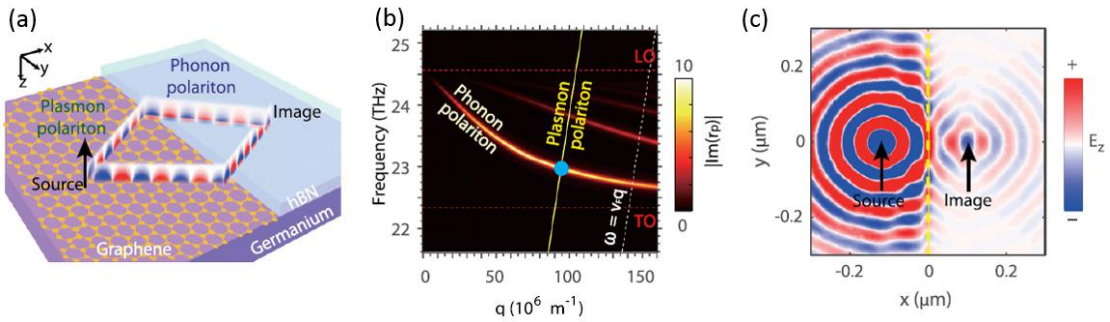

Figure.1-8 (a) Schematics of graphene-BN heterostructure supporting negative refraction effect. (b) Dispersion of phonon polaritons in BN. (c) Electric field distribution under the excitation of a dipole source [56].

Also, it is possible to construct heterostructures using different 2D vdW materials without the 'lattice mismatch' being a hurdle for weak van der Waals interactions, and in this case more complex dispersion relations and hybridization of different kinds of polaritons need to be considered. For example, graphene-BN heterostructure has been demonstrated to achieve negative refraction effects making use of its hyperbolic behavior in the reststrahlen bands [56] (Fig.1-8) and proved to be

an excellent platform for graphene plasmonics with low plasmon damping and strong field confinement [4].

1.2.2 Polaritons in two-dimensional materials beyond graphene

Graphene has paved the way for the exploration of other 2D materials with exotic physical properties [31,33,58]. For example, gapped Dirac material such as semiconducting transition metal dichalcogenides (TMD), especially molybdenum disulfide (MoS_2) and tungsten diselenide (WSe_2) are proved to be promising candidates of emitting devise which cannot be achieved with semi-metallic graphene. Furthermore, TMDs are reported to response differently to circular polarized light due to selective pumping of valley carries [59], which result in a non-zero transverse conductivity unlike the isotropic plasmons in graphene (i.e. $\sigma_{xy} = -\sigma_{yx} \neq 0$ for conductivity tensor $\bar{\bar{\sigma}} = [\sigma_{xx}, \sigma_{xy}; \sigma_{yx}, \sigma_{yy}]$ [33]), as shown in Figure.1-9.

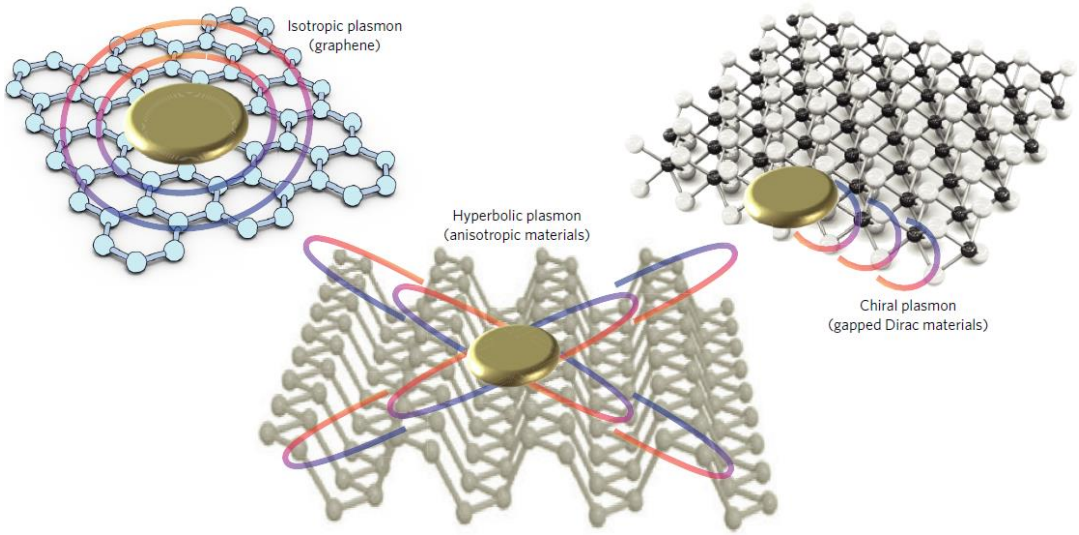

Figure.1-9 Schematics of 2D plasmonic materials with different optical conductivities [33].

On the other hand, hyperbolic anisotropic 2D materials such as black phosphorus [60,61] exhibit permittivities of opposite signs along different directions

(i.e. $Im(\sigma_{xx}) \cdot Im(\sigma_{yy}) < 0$) which can give capacitive and inductive optical responses along the two Cartesian axes. The dispersion can be given as [62]:

$$\frac{q_x^2}{Im(\sigma_{yy})} + \frac{q_y^2}{Im(\sigma_{xx})} = 2p\omega\left(\frac{\varepsilon_0}{Im(\sigma_{xx}) \cdot Im(\sigma_{yy})} - \frac{\mu_0}{4}\right) \quad (1.2)$$

where $p = \sqrt{q_x^2 + q_y^2 - k_0^2}$. The isofrequency contour in the purely anisotropic case (i.e. $Im(\sigma_{xx}), Im(\sigma_{yy}) > 0$) will take an quasielliptic form (blue line in Fig.1-10), while for the hyperbolic case ($Im(\sigma_{xx}) \cdot Im(\sigma_{yy}) < 0$) the k surface turns into a hyperbola form (red and green lines in Fig.1-10) and polaritons can only propagate along the direction of the hyperbola asymptotes defined by $y = \pm x\sqrt{|\, Im(\sigma_{yy}) / Im(\sigma_{xx})|}$ [62]. This means that the plasmon beams are localized to a certain direction and won't spread laterally when propagating. X. Wang et al. experimentally verified the huge in-plane anisotropy of monolayer black phosphorus by polarization-resolved photoluminescence spectroscopy (Fig.1-10 (c)) [61].

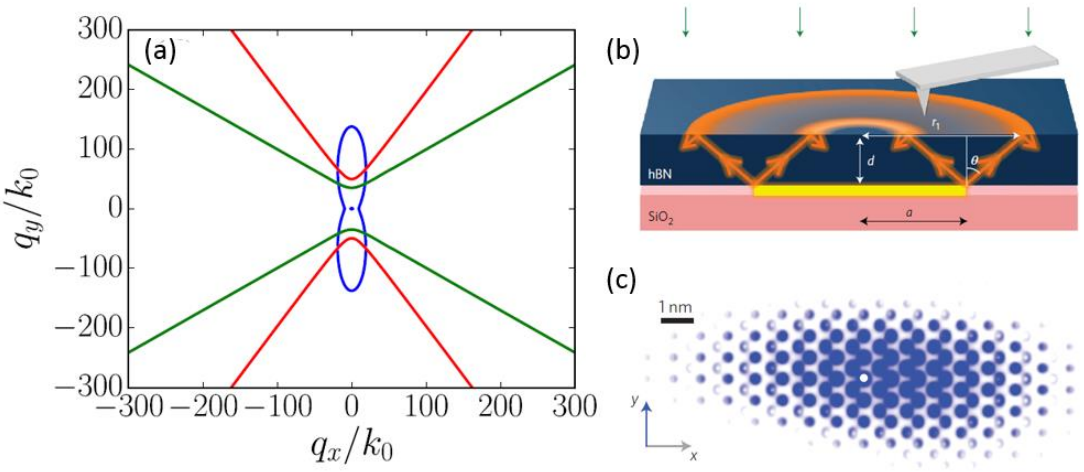

Figure.1-10 (a) Isofrequency contours of 2D materials [62]. (b) Schematics of hBN 'hyperlens' [63]. (c) The squared electron wavefunction of ground-state exciton of monolayer black phosphorus showing strong polarization along the x direction [61].

Also, the direction of the group velocity which is orthogonal to the k surface

can be negative in a natural hyperbolic material. For example, in Ref. [63] the author make use of the hyperbolic phonon polaritons in hexagonal boron nitride (hBN) to construct a 'hyper-focusing lens' to image an Au nanodisk (Fig.1-10 (b)). hBN used in this example is a natural hyperbolic material in the mid-infrared region with hyperbolic dispersion in the first and second reststrahlen band where the in-plane and out-plane permmitivities have opposite signs. Examples of graphene-hBN heterostructures which involves the hybrid phasmon-phonon polaritons have been discussed in the former part.

1.3 Manipulating light at the nanoscale

Manipulating light at the nanoscale in plasmonics system is complemented by the powerful tools of metamaterials and transformation optics (TO). Below we will briefly introduce these two closely related fields and some of the important applications.

1.3.1 Metamaterial and metasurface

Metamaterial are rationally engineered artificial material consisting of periodically arranged meta-atoms which can achieve fascinating properties that are unattainable in nature, such as negative permeability and negative refractive index, leading to the intriguing phenomenon of negative refraction. The word 'meta' stems from Greek, meaning that metamaterials possess properties beyond conventional materials. In 2001, D. R. Smith et al. [64] experimentally demonstrate negative refraction effect at microwave frequencies based on periodic unit cell comprised of copper strips for negative permittivity and split-ring-resonators (SRR) for negative magnetic permeability. Besides negative refraction media, later in 2008 researchers also reported experimental realizations of singular media which are characterized by extreme constitutive parameters such as the epsilon-near-zero (ENZ) media [65,66]. Moreover, the development of the theory of transformation optics first proposed by

John Pendry [67] and Ulf Leonhardt [68] in 2006 provides theoretical guidance on how to design the constituent parameters for novel electromagnetic devices such as invisibility cloaks [67-69], beam splitters [70] and field rotators [71], and thereby greatly accelerates the practical application of metamaterials.

Recently, the idea of artificial metamaterials with unusual electromagnetic properties gives another boost to the field of plasmonics. After successful demonstration of negative refractive index metamaterials in microwave frequencies introduced above, the concept of metamaterials has been widely adopted in optics research, owing to the development of subwavelength nanofabrication and nanoimaging techniques. Besides SRR structure which has been extensively studied in the microwave regime, in the optical regime the so-called ultrathin metasurfaces which are the two-dimensional version of metamaterial can be made of spatially varying nanoparticles [72] or apertures [73] or thin films. In the optical regime, the realization of negative refraction which refers to the phenomenon first described by Veselago in 1968 [74] that the refracted beam stay on the same side of the normal with the incident beam, in contrast to the conventional Snell's law, is an important step towards sub-wavelength imaging beyond the diffraction limit. After first theoretically proposed by Pendry that a slab of negative index media can act as a 'perfect lens' [75], N. Fang et al. have demonstrated that optical evanescent waves can be enhanced in a silver superlens [76]. Besides the abnormal negative refraction effect, designer metasurfaces can also support other complex functionalities based on the ability to modify the phase, amplitude and polarization of light, such as holography [72] , flat lens [77] and directional couplers [73,78].

Also, in the terahertz and infrared regime, metamaterial based on nanostructured 2D material were experimentally and theoretically studied in the past

few years. For example, in Ref. [79] the author experimentally visualize the highly confined in-plane hyperbolic polariton supported by a metasurface made of hBN ribbons (Fig.1-11 (a)). In Ref. [36] the author demonstrate the tunability of metamaterial made up of graphene ribbon arrays via changing the ribbon's width and carrier doping level (Fig.1-11 (b)). In Ref. [80], monolayer graphene modulated by electrical gating over a ridged ground plane is investigated for subwavelength focusing and imaging (Fig.1-11 (c)).

With the help of the effective medium theory [81,82], the effective constituent parameters of the ribbons introduced above or other complex structure can be easily calculated with size parameters of the patterned structure as the input. Also, the effective medium theory allows researcher to inversely determine the geometric parameters suitable for the device under study.

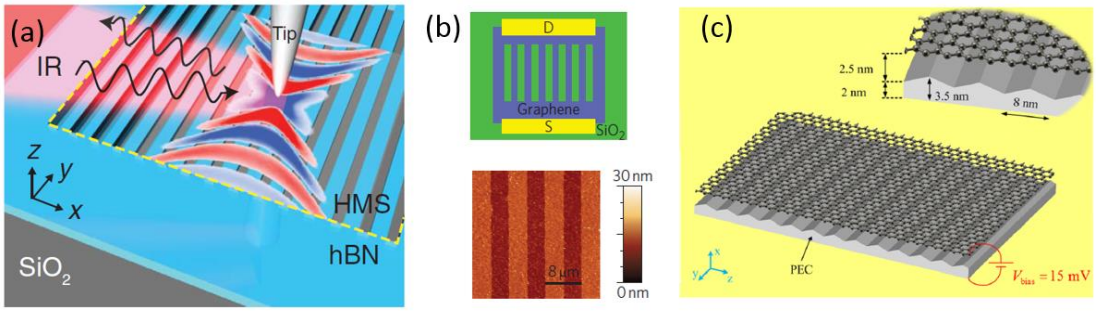

Figure.1-11 (a) Schematic of the experimental visualization of hyperbolic polaritons in hBN ribbon metasurface [79]. (b) Schematics (upper) and the atomic force microscopy image (lower) of graphene ribbon array [36]. (c) Modulated graphene monolayer for THz planar hyperlens [80].

1.3.2 Transformation optics

The creation of more and more complex plasmonic structures such as clusters, dimers, nanoshells, ring/disk nanocavities has led to the development of analytical and numerical tools to study the interaction between nanoparticles. Prodan et al. proposed a plasmon hybridization model (Figure.1-12) to describe the interaction between individual particle plasmons in a complex nanostructure [83].

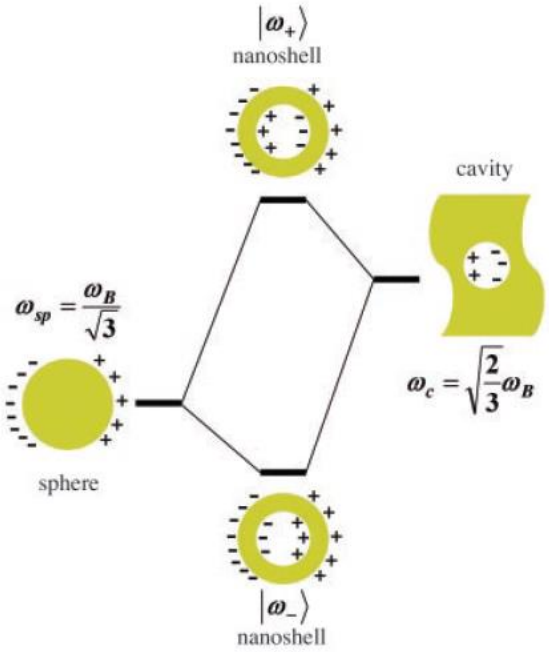

Figure.1-12 plasmon hybridization model describing the coupling between the sphere and cavity plasmons in metal nanoshells [83].

In this model, in analogy to the molecular orbital theory, the coupling of two or more plasmonic nanoparticles leads to the splitting into a lower energy bonding mode and a higher energy antibonding mode. However, albeit elegant, the plasmon hybridization picture is a limited tool and the calculation of the full analytical solution of the optical response still relies on numerical simulations.

Normally, for complex nanostructures containing several individual structures with asymmetry, the analytical solution of their optical response can be calculated using classical Mie scattering theory combined with multiple scattering. However, this

approach involves treatment of higher-order cylindrical harmonics which may suffers from overwhelm computational costs, especially when tackle structures with singularities down to the sub-nanometre level. In this situation, analytical approach based on transformation optics has been proposed to describe the plasmonic response in these complex nanostructures [22,84-86]. The idea of transformation optics is based on the invariance of Maxwell's equations under coordinate transformations, as long as the permittivity and permeability are modified as [87]:

$$\varepsilon'^{i'j'} = [\det(\Lambda)]^{-1}\Lambda_i^{i'}\Lambda_j^{j'}\varepsilon^{ij} \tag{1.3}$$

$$\mu'^{i'j'} = [\det(\Lambda)]^{-1}\Lambda_i^{i'}\Lambda_j^{j'}\mu^{ij} \tag{1.4}$$

where $\varepsilon, \mu, \varepsilon', \mu'$ are the permittivity and permeability in the original and transformed frame, respectively, and Λ is the first derivative of the transformation.

The significance of this property is two-fold: firstly, as mentioned in the last part, we can arbitrarily shape the trajectory of rays by simple coordinates distortion. In particular, the rays can be steered away from the region we want to conceal [67] to form an invisibility cloak. Secondly, the applicability of transformation optics to analytically solve the optical response of complex nanostructure under a more symmetric transformed frame renders it a powerful tool for precise design of light-harvesting nanoparticle with geometrical singularities, and brings about more physical insight by reveal the hidden symmetry [88]. For example, in Ref. [22] the plasmonic interaction in a cylindrical dimer is studied by relating the original structure to two semi-infinite slabs excited by a dipole source in the planer cavity through exponential transformation. It can be clearly seen in the absorption cross section (lower panel of Fig.1-13 (a)) that higher order modes arise and finally form a continuum spectrum as the two nanoparticles approach each other.

Interestingly, in transformation optics, one “mother” structure can be related to a numbers of “daughter” structures, following the general rule that infinite “mother” structure corresponding to “daughter” structure with sharp singularities [85,86] while finite “mother” structure corresponding to blunt “daughter” structure without singularities [91,92]. For instance, as shown in Fig.1-13 (c), the same planar waveguide structure with dipole excitation as that in Fig.1-13 (a) can also be related to a crescent and a kissing cylinder structure with large field enhancement at the geometrical singularities [90]. Moreover, the conformal transformation has also been extended to three-dimensional regime, where a pair of nanosphere is related to an annuals system via inversion transformation, and anomalous modes can be observed which are not found with cylindrical dimers [89] (Fig.1-13 (b)).

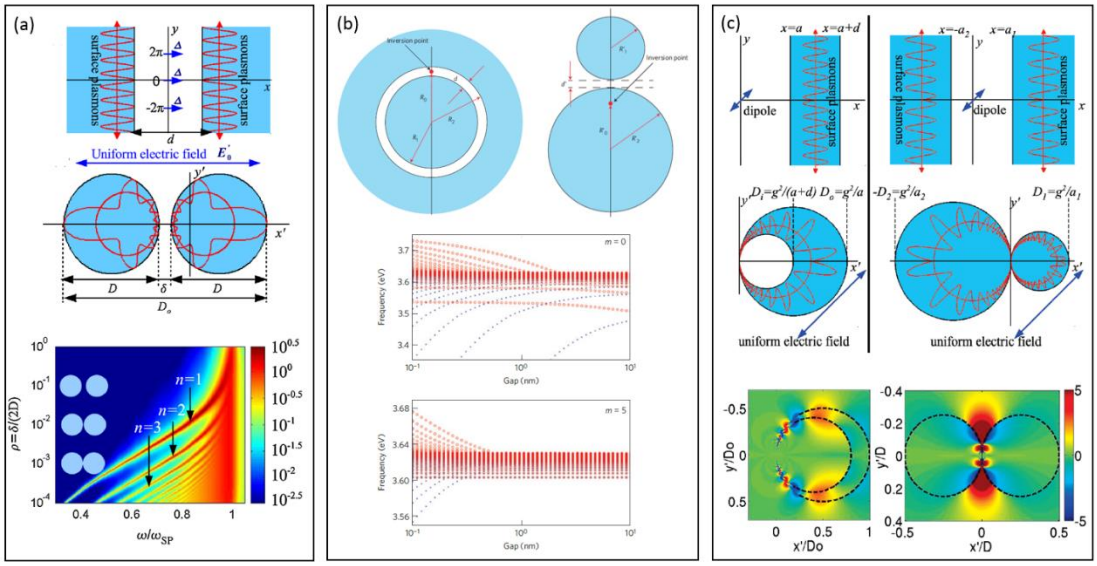

Figure.1-13 (a) Upper panel: transformation between a planar waveguide and cylindrical dimer. Lower panel: absorption cross section against the gap size [22]. (b) Upper panel: annulus system and spherical dimer related by conformal mapping. Lower panel: modes of spherical dimer consist of two 5 nm radius spheres against different separations [89]. (c) Upper panel: a thing metallic slab and two semi-infinite slabs relating to a crescent and a pair of kissing cylinders. Lower panel: Normalized electric field distribution [90].

Most of the examples above assume that the system is small with respect to the wavelength. However, when structure size increases and goes beyond the so-called quasistatic limit, radiation corrections need to be included to account for the radiative loss that cannot be omitted anymore, which can be done by placing an extra fictive absorbing partial in the planar cavity [93]. On the other hand, nonlocal effect arises accompanies the size reduction of the structure, and nonlocal corrections need to be included when the system's size reaching a few nanometers in diameter [94,95]. Also, inspired by the prosperous field of graphene plasmonics and other 2D polaritons, TO has been exploited to design devices such as splitter, 2D Luneburg lens [40] and gratings [96] for light manipulation in the infrared regime based on monolayer graphene with spatially varying conductivity patterns.

1.4 Organization of the thesis

The main body of this thesis contains three parts. The first section studies the interaction between two graphene-coated cylinders based on a modified transformation optics method and theoretically predict the polarization independent broadband spectrum response and multiple Fano dips. The second section studies the negative reflection effects supported by an ultrathin metasurface consisting of perpendicularly concatenated 2D material. The third section studies single- and double-layer nonreciprocal graphene sheets biased with drift current and demonstrates a unidirectional waveguide design. The last chapter summarized the main work of this thesis and suggested the prospects of subsequent work in the future.

Chapter 2 Interaction between graphene-coated nanowires revisited with transformation optics

2.1 Background and motivation

Graphene plasmonics characterized with low losses, tubability and tight confinement [97] makes them favorable substitutes to conventional plasmons in noble metal and excellent platform for nanophotonic applications. Furthermore, for applications such as biomolecules' detection [30], it is of great significance to move the operating frequency to the terahertz regime from the optical regime. Structures with a variety of different geometries have been put forward to make use of these properties, such as graphene nanodisks [48], nanoribbon arrays [98,99], and graphene conductivity gratings [96].

Among these various proposals, graphene-coated nanoparticles have attracted considerable attention for the exceptional optical phenomena originate from the interaction of the individual core and shell plasmons, such as superscattering peaks [51] and invisibility dips [49]. However, most of these studies are mainly focused on single particle coated with the graphene monolayer, lacking the plasmon hybridization effect manifest in dimer structures which provides extra freedom to tailor the multiple asymmetric Fano dips and field enhancement for light harvesting and sensing applications. In detail, within the plasmon hybridization process for a graphene-coated dimer, the localized surface plasmon (LSP) modes of individual graphene-coated particle couple with each other and split into bonding modes with odd symmetry and antibonding modes with even symmetry, in the same fashion as its metallic counterpart [83]. In Ref. [100], the conversion frequency for second harmonic generation is obtained via the coupled mode formulism for a pair of graphene-coated nanowires. However, numerical finite element method (FEM) is exploited for the calculation of

the eigen mode patterns and mode indices in this work. It is still difficult to obtain full-analytical solutions, which can provide deep physical insights into the hybrid graphene plasmonic systems, whereas the classical Mie scattering theory combined with multiple scattering suffers from overwhelm computational burden when dealing with higher-order cylindrical harmonics and extremely small separations.

To tackle these shortcomings, a powerful analytical method called transformation optics [87,101,102] has been put forward for the description of optical responses of complex plasmonic systems, especially those contain geometrical singularities, such as kissing cylinders [90] and crescents [86], which are difficult to deal with via conventional methods. By relating the original singular geometry to another geometry with more symmetry, computational efficiency is largely enhanced through the reduction of the size of the reflection matrices, and more physical insights are provided via the disclosure of the hidden geometry [88]. However, since the surface conductivity of graphene is not preserved like the in-plane permittivity when perform the conformal mapping, we cannot directly apply the conventional transformation optics for the calculation of the core-shell dimer structure we want to study here.

Therefore, in this work, a highly non-uniform surface conductivity of the graphene layer is introduced in the transformed coordinates to develop a customized transformation optics approach. The scattering spectrum is analytically calculated based on this customized TO approach and are then verified through comparison with the simulation results. In detail, inversion mapping is adopted here for the reason that it can maps the cylinder pair into a symmetric annulus system, but with spatially variant graphene conductivities.

We demonstrate that the graphene-coated dimer has a broadband response in terms of the scattering and absorption spectrum, and unlike the traditional plasmonic

dimers whose modes distribution pattern is closely related to the polarization [103], here the broadband response is polarization independent and can be obtained no matter the incident wave is $\hat{x}$ or $\hat{y}$ polarized.

2.2 Solve for the optical response of graphene-coated structures

In this part, we investigate the optical properties of some graphene structures with gradually increasing geometrical complexity, from a monolayer graphene sheet and a single graphene cylinder to a pair of graphene cylinders that we are interested in. The surface conductivity σ_s is adopted to describe graphene's optical properties, whose relationship with the bulk permittivity is given by

$$\varepsilon_{\text{bulk}} = 1 + i\frac{\sigma_s}{\omega\varepsilon_0\Delta d} \tag{2.1}$$

where Δd is an infinitesimal distance characterize the layer thickness. The governing equation for the electromagnetic fields can be expressed as:

$$\begin{cases} \nabla\times\bar{H} = -i\omega\varepsilon_0\bar{E} + \sigma_s\bar{E}\delta(F(\mathbf{r})) \\ \nabla\times\bar{E} = i\omega\mu_0\bar{H} \end{cases} \tag{2.2}$$

Equation (2.2) indicates that the presence of the graphene will introduce an effective surface current at the boundary, which may result in new plasmon modes. In the following, we will illustrate this point by considering three examples.

2.2.1 Monolayer graphene sheet

We first consider a monolayer graphene sheet placed at y = 0, as shown in the following figure:

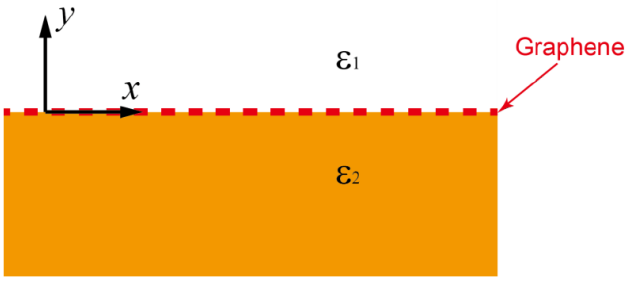

Figure.2-1 Schematics of a monolayer graphene placed at the interface of two kinds of materials.

For surface plasmons in transverse magnetic (TM) modes, we can write the electromagnetic fields above and below the graphene sheet as:

$$\begin{aligned} H_z^{\mathrm{I}} &= A^{\mathrm{I}} \exp(-k_y^{\mathrm{I}} y + ik_x x), \\ E_x^{\mathrm{I}} &= -\frac{ik_y^{\mathrm{I}} A^{\mathrm{I}}}{\omega\varepsilon_0\varepsilon_1} \exp(-k_y^{\mathrm{I}} y + ik_x x), \\ E_y^{\mathrm{I}} &= -\frac{k_x A^{\mathrm{I}}}{\omega\varepsilon_0\varepsilon_1} \exp(-k_y^{\mathrm{I}} y + ik_x x), \end{aligned} \tag{2.3}$$

for y > 0 while for y < 0:

$$\begin{aligned} H_z^{\mathrm{II}} &= A^{\mathrm{II}} \exp(k_y^{\mathrm{II}} y + ik_x x), \\ E_x^{\mathrm{II}} &= -\frac{ik_y^{\mathrm{II}} A^{\mathrm{II}}}{\omega\varepsilon_0\varepsilon_2} \exp(k_y^{\mathrm{II}} y + ik_x x), \\ E_y^{\mathrm{II}} &= -\frac{k_x A^{\mathrm{II}}}{\omega\varepsilon_0\varepsilon_2} \exp(k_y^{\mathrm{II}} y + ik_x x), \end{aligned} \tag{2.4}$$

where $k_y^{\mathrm{I}} = \sqrt{k_x^2 - \varepsilon_1 k_0^2}$ and $k_y^{\mathrm{II}} = \sqrt{k_x^2 - \varepsilon_2 k_0^2}$. Through imposing the boundary conditions at the boundaries, we have the following equations:

$$\begin{aligned} \frac{-k_y^{\mathrm{I}} A^{\mathrm{I}}}{\varepsilon_1} &= \frac{k_y^{\mathrm{II}} A^{\mathrm{II}}}{\varepsilon_2}, \\ A^{\mathrm{I}} &= A^{\mathrm{II}} \left(1 + \frac{i\sigma_s k_y^{\mathrm{II}}}{\omega\varepsilon_0\varepsilon_2} \right), \end{aligned} \tag{2.5}$$

which in turns yield:

$$\frac{\varepsilon_1}{k_y^{\mathrm{I}}} + \frac{\varepsilon_2}{k_y^{\mathrm{II}}} = -\frac{i\sigma_s}{\omega\varepsilon_0} \tag{2.6}$$

If the graphene layer is absent, the existence of surface plasmon excitation requires $Re(\varepsilon_1)$ and $Re(\varepsilon_2)$ have different sign. Nevertheless, Eq. (2.6) indicates that as long as σ_s has a positive imaginary part, the excitation of surface modes is possible even when

ε_1 and ε_2 are both positive. More interestingly, in the quasistatic limit (where $k_y^{\mathrm{I}} = k_y^{\mathrm{II}} = k_x$), Eq. (2.6) reduces to:

$$k_x = \frac{i\omega\varepsilon_0(\varepsilon_1 + \varepsilon_2)}{\sigma_s} \tag{2.7}$$

Interestingly, we note that the surface plasmon modes do not degenerate at a single frequency, contrary to the case of a single metal surface (where all the plasmon modes are found to merge at the surface plasmon frequency).

To calculate the SPP dispersion, we must first determine σ_s. From the Kubo formula the conductivity of graphene can be described by summing up the contributions from the intraband and interband transitions of electrons $\sigma_s = \sigma_{intra} + \sigma_{inter}$, where the intra- and inter- band contributions can be expressed as [90]

$$\sigma_{\text{intra}} = i\frac{e^2 k_B T}{\pi\hbar^2(\omega + i2\Gamma)}\left(\frac{\mu_c}{k_B T} + 2\ln(e^{-\mu_c/k_B T} + 1)\right) \tag{2.8}$$

$$\sigma_{\text{inter}} = \frac{ie^2}{4\pi\hbar}\ln\left(\frac{2|\mu_c| - (\omega + i2\Gamma)\hbar}{2|\mu_c| + (\omega + i2\Gamma)\hbar}\right) \tag{2.9}$$

where e is the element charge, k_B is the Boltzmann constant, Γ is the phenomenological scattering rate, and μ_c is the chemical potential which can be tuned through the gate voltage and/or chemical doping. Here in following calculations we assume T=300 k (i.e. room temperature), the scattering rate $\Gamma = 0.11$ meV, and the chemical potential is 0.5 eV.

Figure.2-2 plots σ_s as a function of the frequency from 1 to 20 THz (wavelength from 15-300 μm), where we can see its imaginary part is positive over a broad frequency band.

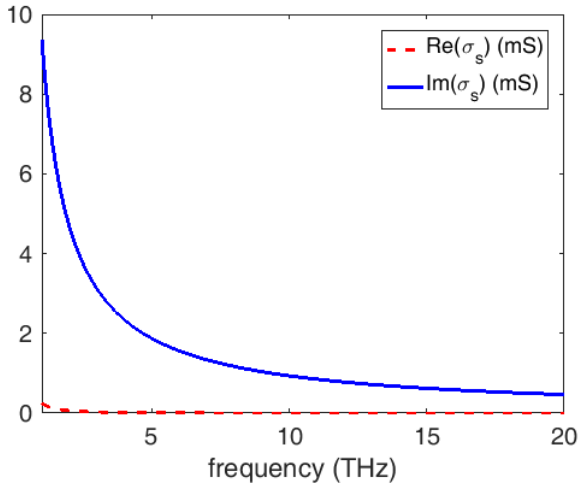

Figure.2-2 Graphene surface conductivity at 1-20 THz calculated by the Kubo formula.

In figure below (Fig.2-3), the SPP dispersion diagram is plotted for monolayer graphene with the above surface conductivity and $\varepsilon_1 = \varepsilon_{air} = 1$, $\varepsilon_2 = \varepsilon_{glass} = 2.1025$, where r is the Fresnel reflection coefficient for p-polarized light. The polariton's dispersion is hidden in the denominator of r, that's why the maximum of pole of r corresponds to the eigenmodes of polaritons.

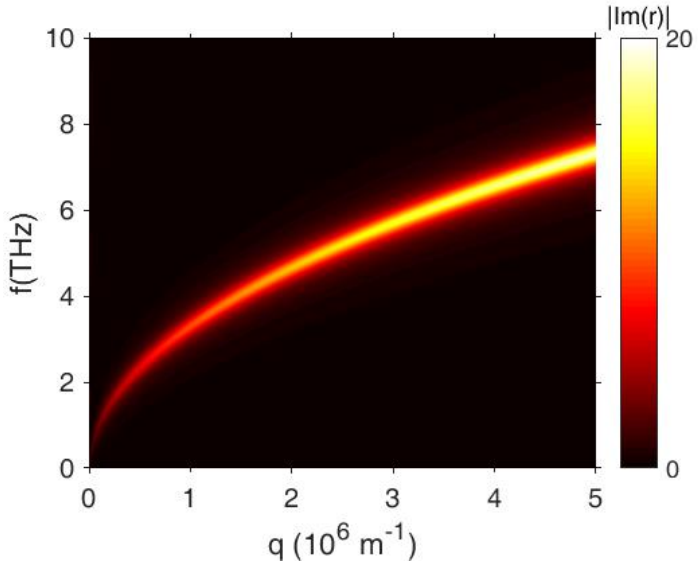

Figure.2-3 Graphene dispersion diagram obtained by plotting the imaginary part of the reflection coefficient.

2.2.2 Single graphene-coated cylinder

Now, we consider the scattering of a small dielectric cylinder covered by a monolayer graphene, as shown in Figure.2-4. We shall make an assumption that the core material in Fig.2-4 is made up of homogeneous dielectrics with $\varepsilon_s = \varepsilon_{glass} = 2.1025$, and the core-shell structure is surrounded by homogeneous material with $\varepsilon_b = \varepsilon_{air} = 1$.

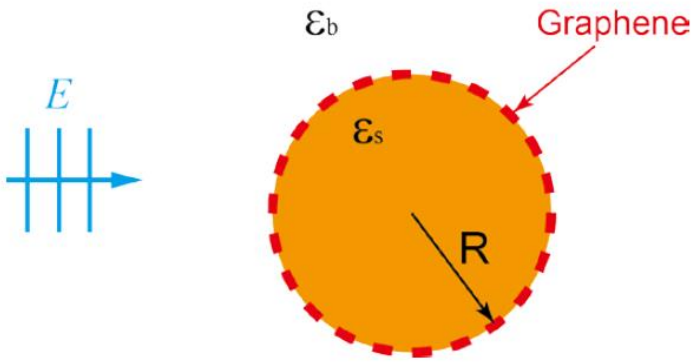

Figure.2-4 Schematic of a dielectric cylinder covered by monolayer graphene.

For TM illumination (i.e. the magnetic field polarized along the axial direction), the electromagnetic fields outside and inside the cylinder can be written as:

$$\begin{cases} H_z^{out} = \sum_{n=-\infty}^{+\infty}\left[a_n^s J_n\left(\sqrt{\varepsilon_b}k_0\rho\right)+a_n^{sca}H_n^{(1)}\left(\sqrt{\varepsilon_b}k_0\rho\right)\right]e^{in\varphi} \\ E_\varphi^{out} = -\dfrac{ik_0}{\omega\varepsilon_0\sqrt{\varepsilon_b}}\sum_{n=-\infty}^{+\infty}\left[a_n^s J_n'\left(\sqrt{\varepsilon_b}k_0\rho\right)+a_n^{sca}H_n^{(1)\prime}\left(\sqrt{\varepsilon_b}k_0\rho\right)\right]e^{in\varphi},\ \text{for } \rho>R \\ E_\rho^{out} = -\dfrac{n}{\omega\varepsilon_0\varepsilon_b\rho}\sum_{n=-\infty}^{+\infty}\left[a_n^s J_n\left(\sqrt{\varepsilon_b}k_0\rho\right)+a_n^{sca}H_n^{(1)}\left(\sqrt{\varepsilon_b}k_0\rho\right)\right]e^{in\varphi} \end{cases} \quad (2.10)$$

$$\begin{cases} H_z^{in} = \sum_{n=-\infty}^{+\infty} a_n^{in} J_n\left(\sqrt{\varepsilon_s}k_0\rho\right)e^{in\varphi} \\ E_\varphi^{in} = -\dfrac{ik_0}{\omega\varepsilon_0\sqrt{\varepsilon_s}}\sum_{n=-\infty}^{+\infty} a_n^{in} J_n'\left(\sqrt{\varepsilon_s}k_0\rho\right)e^{in\varphi},\ \text{for } \rho<R \\ E_\rho^{in} = -\dfrac{n}{\omega\varepsilon_0\varepsilon_s\rho}\sum_{n=-\infty}^{+\infty} a_n^{in} J_n\left(\sqrt{\varepsilon_s}k_0\rho\right)e^{in\varphi} \end{cases} \quad (2.11)$$

where $a^s = i^n$ is the expansion coefficient associated with the incident TM wave. The boundary equations can be written as:

$$\begin{aligned} a_n^s J_n'\left(\sqrt{\varepsilon_\mathrm{b}}k_0 R\right) + a_n^{sca} H_n^{(1)\prime}\left(\sqrt{\varepsilon_\mathrm{b}}k_0\rho\right) &= \sqrt{\frac{\varepsilon_\mathrm{b}}{\varepsilon_\mathrm{s}}} a_n^{in} J_n'\left(\sqrt{\varepsilon_\mathrm{s}}k_0\rho\right) \\ a_n^s J_n\left(\sqrt{\varepsilon_\mathrm{b}}k_0 R\right) + a_n^{sca} H_n^{(1)}\left(\sqrt{\varepsilon_\mathrm{b}}k_0\rho\right) &= a_n^{in}\left[J_n\left(\sqrt{\varepsilon_\mathrm{s}}k_0\rho\right) + \frac{i\sigma_\mathrm{s}k_0}{\omega\varepsilon_0\sqrt{\varepsilon_\mathrm{s}}} J_n'\left(\sqrt{\varepsilon_\mathrm{s}}k_0\rho\right)\right] \end{aligned} \tag{2.12}$$

The scattering coefficient a_n^{sca} can be obtained by solving Eq. (2.12):

$$a_n^{sca} = a_n^s \frac{J_n'(\xi_\mathrm{b})\left[\sqrt{\varepsilon_\mathrm{s}} J_n(\xi_\mathrm{s}) + \frac{i\sigma_\mathrm{s}k_0}{\omega\varepsilon_0} J_n'\left(\xi_\mathrm{s}\right)\right] - \sqrt{\varepsilon_\mathrm{b}} J_n(\xi_\mathrm{b}) J_n'(\xi_\mathrm{s})}{\sqrt{\varepsilon_\mathrm{b}} J_n'(\xi_\mathrm{s}) H_n^{(1)}\left(\xi_\mathrm{b}\right) - \left[\sqrt{\varepsilon_\mathrm{s}} J_n(\xi_\mathrm{s}) + \frac{i\sigma_\mathrm{s}k_0}{\omega\varepsilon_0} J_n'\left(\xi_\mathrm{s}\right)\right] H_n^{(1)\prime}\left(\xi_\mathrm{b}\right)} \tag{2.13}$$

where we have introduced two constants $\xi_b = \sqrt{\varepsilon_b}k_0 R$ and $\xi_s = \sqrt{\varepsilon_s}k_0 R$. Using the asymptotic form of cylindrical Bessel and Hankel functions [104], we can rewrite Eq. (2.13) in the quasistatic limit:

$$a_n^{sca} = a_n^s\left(\frac{i\pi\xi_\mathrm{b}^{2n}}{2^{2n} n!(n-1)!}\right)\left(\frac{\varepsilon_\mathrm{s} - \varepsilon_\mathrm{b} + \frac{in\sigma_\mathrm{s}}{\omega\varepsilon_0 R}}{\varepsilon_\mathrm{s} + \varepsilon_\mathrm{b} + \frac{in\sigma_\mathrm{s}}{\omega\varepsilon_0 R}}\right) \tag{2.14}$$

Equation (2.14) indicates that the resonance condition for surface plasmon excitation is:

$$\sigma_s = \frac{i\omega\varepsilon_0 R(\varepsilon_\mathrm{s} + \varepsilon_\mathrm{b})}{n} \tag{2.15}$$

while the cloaking condition (i.e. zero scattering) is:

$$\sigma_s = \frac{i\omega\varepsilon_0 R(\varepsilon_\mathrm{s} - \varepsilon_\mathrm{b})}{n} \tag{2.16}$$

For example, for a graphene-coated glass with $\varepsilon_s = 2.1025$, $\varepsilon_b = 1$ and radius equal to 1 μm under TM illumination, the absorption and scattering cross sections can be plotted as:

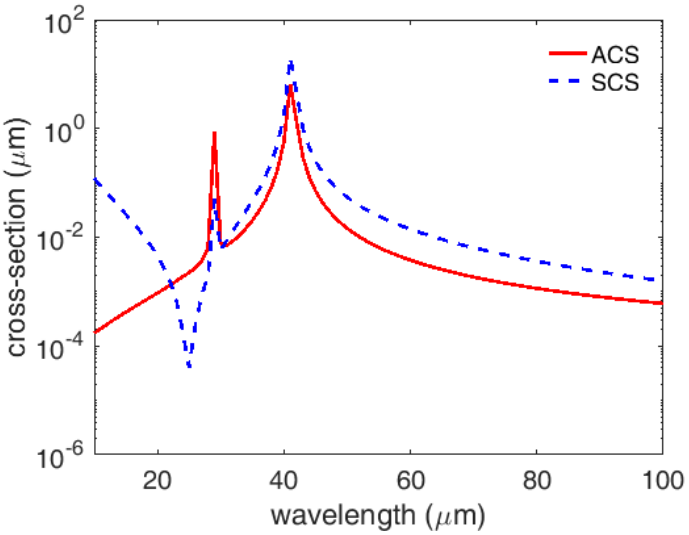

Figure.2-5 Absorption cross section (ACS) and scattering cross section (SCS) of a single graphene-coated glass cylinder of radius 1 μm.

The cloaking frequency (i.e. the prominent dip in the scattering spectrum) can be inferred form Fig.2-5 to be around 12 THz (wavelength equal to 25 μm), which is consistent with eq. (2.16) taking n=1, which means the dipolar mode dominates and the size of the cylinder is small enough to apply the quasistatic approximation.

2.2.3 Graphene-coated cylinder pair

Now we consider the optical responses of graphene cylinder pair, as show in Fig.2-6 (a). Instead of the classic Mie scattering theory and multiple scattering, here we exploit the transformation optics methods to treat the problem. As illustrated in Fig.2-6, firstly, we map the original dimer system in Fig.2-6 (a) into a much more symmetric multilayer core-shell system (Fig.2-6 (b)) with the following conformal mapping formulism,

$$\xi' = \frac{g^2}{\xi - R_0} \tag{2.17}$$

where $\xi = x + iy$ and $\xi' = x' + iy'$. Via this transformation, points at infinity are mapped to the inversion point, R_0. Similar inversion mapping has also been adopted to

study metallic nanosphere dimers [89].

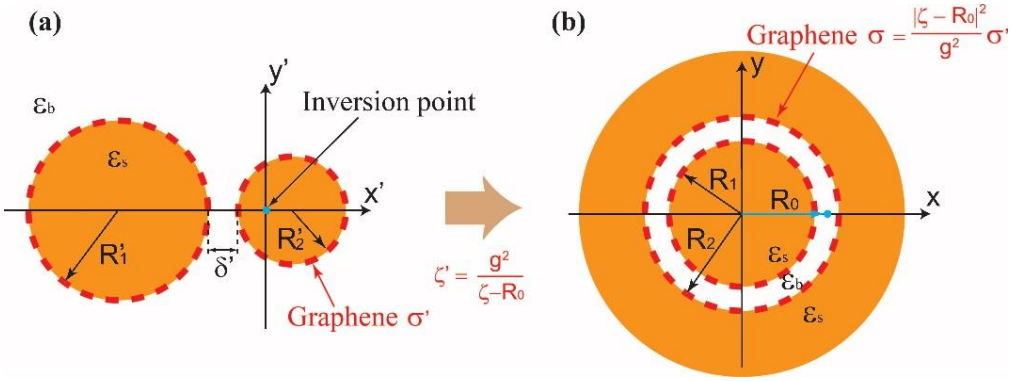

Figure.2-6 Schematics of (a) The original frame comprised of a pair of core-shell nanowires and (b) the annuals structure obtained after performing the inversion transformation. Reprinted with permission from ref. [105] © 2017 Optical Society of America.

Under this transformation, the relation between R_1', R_2', δ' and R_0, R_1, R_2 can be given as:

$$\begin{cases} \dfrac{g^2}{R_1 - R_0} + \dfrac{g^2}{R_1 + R_0} = -2R_1' \\ \dfrac{g^2}{R_2 - R_0} + \dfrac{g^2}{R_2 + R_0} = 2R_2' \\ \dfrac{g^2}{R_1 + R_0} - \dfrac{g^2}{R_2 + R_0} = \delta' \end{cases} \tag{2.18}$$

Eq. (2.18) yields:

$$\begin{cases} R_0 = \dfrac{g^2(\delta' + R_1' + R_2')}{\sqrt{\delta_1'(\delta' + 2R_1')(\delta' + 2R_2')(\delta' + 2R_1' + 2R_2')}} \\ R_1 = -\dfrac{g^2}{2R_1'} + \sqrt{\dfrac{g^4}{4R_1'^2} + R_0^2} \\ R_2 = \dfrac{g^2}{2R_2'} + \sqrt{\dfrac{g^4}{4R_2'^2} + R_0^2} \end{cases} \tag{2.19}$$

Under the inversion transformation, the in-plane permittivity of the material is unchanged [106,107]. Since $\sigma = \varepsilon \cdot \Delta d$ (where Δd is an infinitesimal distance), we can

obtain a non-uniform conductivity in accordance with Δd, as illustrated in Fig.2-7. Assume that in the original coordinates system we have $\Delta d' = \xi_0' - \xi'$, in the transformed frame we have

$$\Delta d = \xi_0 - \xi = \frac{g^2}{\xi_0'} - \frac{g^2}{\xi'} = -\frac{g^2 \Delta d'}{\xi'^2} = -\frac{(\xi + R_0)^2 \Delta d'}{g^2} \tag{2.20}$$

Hence

$$\sigma = \frac{|\xi - R_0|^2}{g^2} \sigma' = \frac{\rho^2 + R_0^2 - 2\rho R_0 \cos\varphi}{g^2} \sigma' \tag{2.21}$$

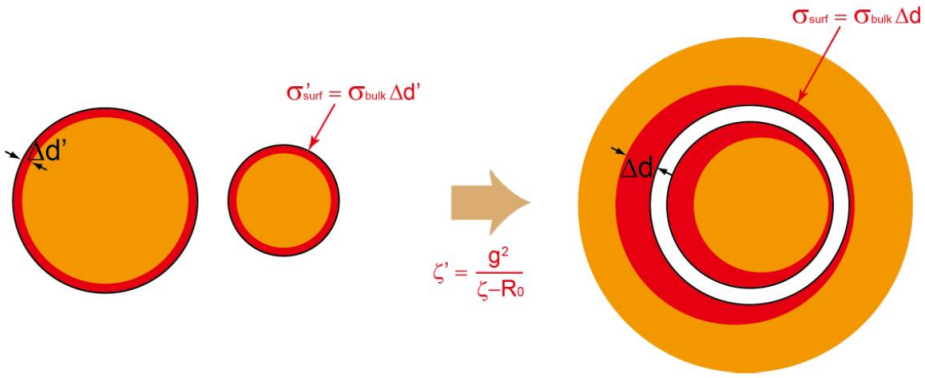

Figure.2-7 Illustration of how the surface conductivity is transformed under the transformation.

Contrast to previous cases where the electric permittivity of the material is conserved when studying the optical response of metallic cylinder dimer [22,85], eq. (2.21) implies that the graphene layer in the transformed frame possess a spatial dependent conductivity without rotational symmetry, which renders a more complex boundary condition.

Next, we solve for the electrostatic potential $\varphi(\rho)$ in the simplified annulus frame and hence find $\varphi(\rho')$ in the original frame. $\varphi(\rho)$ in the annulus frame can be expressed as

$$\begin{aligned}
&\sum_n a_n^{in}(\rho/R_0)^n,\ \rho < R_1 \\
&\sum_n \left[(a_n^+ + a_n^{s+})(\rho/R_0)^n + a_n^-(\rho/R_0)^{-n}\right],\ R_0 > \rho > R_1 \\
&\sum_n \left[a_n^+(\rho/R_0)^n + (a_n^- + a_n^{s-})(\rho/R_0)^{-n}\right],\ R_2 > \rho > R_0 \\
&\sum_n a_n^{out}(\rho/R_0)^{-n},\ \rho > R_2
\end{aligned} \tag{2.22}$$

where $a_n^{\pm}$ are the unknowns to be solved, $a_n^{s\pm}$ are the source coefficients related to the incident wave, and the exponential expansions are written in the polar coordinate system defined by (ρ, φ) (angle related factors $cosn\varphi$ and $sinn\varphi$ are omitted here) centered at the origin of the Cartesian coordinate system (x, y). R_0 in the denominator of the exponential term is for the purpose of normalization, so as to avoid the situation that the coefficients blow up and complicates the calculation.

It has been demonstrated in literature [91] that the uniform field in the original coordinate system characterized by the potential $\phi^{s\prime} = -x'E_x - y'E_y$ can be expanded as below in the transformed space:

$$\begin{aligned}
\phi^s &= -\frac{g^2(\rho\cos\varphi - R_0)}{\rho^2 + R_0^2 - 2\rho R_0\cos\varphi}E_x + \frac{g^2\rho\sin\varphi}{\rho^2 + R_0^2 - 2\rho R_0\cos\varphi}E_y \\
&= \begin{cases}
\sum_{n=1}^{\infty}\left(\frac{\rho}{R_0}\right)^n (a_n^{s+}\cos n\varphi + b_n^{s+}\sin n\varphi), & \rho < R_0 \\
\sum_{n=1}^{\infty}\left(\frac{\rho}{R_0}\right)^{-n} (a_n^{s-}\cos n\varphi + b_n^{s-}\sin n\varphi), & \rho > R_0
\end{cases}
\end{aligned} \tag{2.23}$$

It can be seen from eq. (2.23) that the incident plane wave in the origin space can be converted to a point dipole in the transformed space. Then by imposing the boundary conditions across the inner and outer radius of the annulus(i.e. $\Delta E_\varphi = 0$ and $\Delta D_\rho = -i\frac{\sigma}{\omega}\frac{\partial E_\varphi}{\rho\partial\varphi}$, deduced from the continuity of the tangential component of the electric field E_φ and the normal component of the electric displacement field D_ρ take into account the surface charge), we have:

$$a_n^{in} = (a_n^{+} + a_n^{s+}) + a_n^{-}\left(\frac{R_0}{R_1}\right)^{2n} \tag{2.24a}$$

$$\begin{aligned}&\sum_n a_n^{in}\left(\varepsilon_s + i\frac{n\sigma_0}{\omega\varepsilon_0 R_1}\frac{R_1^2 + R_0^2 + 2R_0R_1\cos\varphi}{g^2}\right)\begin{pmatrix}\cos n\varphi\\ \sin n\varphi\end{pmatrix}\\ &= \sum_n \varepsilon_b\left[\left(a_n^{+} + a_n^{s+}\right) - a_n^{-}\left(\frac{R_0}{R_1}\right)^{2n}\right]\begin{pmatrix}\cos n\varphi\\ \sin n\varphi\end{pmatrix}\end{aligned} \tag{2.24b}$$

$$a_n^{out} = a_n^{+}\left(\frac{R_2}{R_0}\right)^{2n} + (a_n^{-} + a_n^{s-}) \tag{2.24c}$$

$$\begin{aligned}&\sum_n -a_n^{out}\left(\varepsilon_s + i\frac{n\sigma_0}{\omega\varepsilon_0 R_2}\frac{R_2^2 + R_0^2 + 2R_0R_2\cos\varphi}{g^2}\right)\begin{pmatrix}\cos n\varphi\\ \sin n\varphi\end{pmatrix}\\ &= \sum_n \varepsilon_b\left[a_n^{+}\left(\frac{R_0}{R_1}\right)^{2n} - \left(a_n^{-} + a_n^{s-}\right)\right]\begin{pmatrix}\cos n\varphi\\ \sin n\varphi\end{pmatrix}\end{aligned} \tag{2.24d}$$

Eq. (2.24a-d) can be written as the following matrix equation after manipulation,

$$\mathbf{R}|a\rangle = \mathbf{S}\left(|a^s\rangle + |a^r\rangle\right) \tag{2.25}$$

where $|a\rangle$ and $|a^s\rangle$ are vectors of the scattering and source coefficients. Radiation damping can be taken into account through inserting a fictive absorbing particle denoted by $|a^r\rangle$ [92] in the transform frame. In eq. (2.25) **R** and **S** can be represented as

$$\mathbf{R} = \begin{bmatrix}\mathbf{P-I} & \mathbf{(P+I)\cdot U}\\ \mathbf{(Q+I)\cdot V} & \mathbf{Q-I}\end{bmatrix},\ \mathbf{S} = -\begin{bmatrix}\mathbf{P-I} & 0\\ 0 & \mathbf{Q-I}\end{bmatrix} \tag{2.26}$$

where the diagonal matrices **U** and **V** can be calculated as

$$U_{nn'} = \left(\frac{R_0}{R_1}\right)^{2n}\delta_{n,n'},\ \ V_{nn'} = \left(\frac{R_2}{R_0}\right)^{2n}\delta_{n,n'}, \tag{2.27}$$

And **I** represents an identity matrix, tri-diagonal matrices **P** and **Q** are the main consequences of the spatially dependent conductivity, which is easy to diagonalize and thus only adds minor complexity to the problem:

$$P_{nn'} = \frac{\varepsilon_s}{\varepsilon_0}\delta_{n,n'} + \frac{i\sigma' R_1}{\omega\varepsilon_0\varepsilon_b g^2}\left[n(1+\frac{R_0^2}{R_1^2})\delta_{n,n'} - \frac{(n-1)^2}{n}\delta_{n,n'+1} - \frac{(n+1)^2}{n}\frac{R_0^2}{R_1^2}\delta_{n,n'-1} \right], \tag{2.28}$$

$$Q_{nn'} = \frac{\varepsilon_s}{\varepsilon_0}\delta_{n,n'} + \frac{i\sigma' R_2}{\omega\varepsilon_0\varepsilon_b g^2}\left[n(1+\frac{R_0^2}{R_2^2})\delta_{n,n'} - \frac{(n-1)^2}{n}\delta_{n,n'+1} - \frac{(n+1)^2}{n}\frac{R_0^2}{R_2^2}\delta_{n,n'-1} \right], \tag{2.29}$$

The two tri-diagonal matrices listed above are derived from the trigonometric identities in order to eliminate the dependence of the conductivity on the azimuthal angle φ in the calculation.

Finally, by substituting solutions of above matrix systems, the electrostatic polarizability γ_x and γ_y for $\hat{x}$ and $\hat{y}$ polarized incident wave can be deduced, and the scattering, extinction, and absorption cross-sections can then be written in terms of the polarizabilities as

$$\sigma_{x,y}^{ext} = k_0 \,\mathrm{Im}\left\{\frac{\gamma_{x,y}}{1-ik_0^2\gamma_x/8}\right\}, \sigma_{x,y}^{sca} = \frac{k_0^3}{8}\left|\frac{\gamma_{x,y}}{1-ik_0^2\gamma_{x,y}/8}\right|^2, \tag{2.30}$$
$$\sigma_{x,y}^{abs} = \sigma_{x,y}^{ext} - \sigma_{x,y}^{sca}$$

2.3 Results and discussion

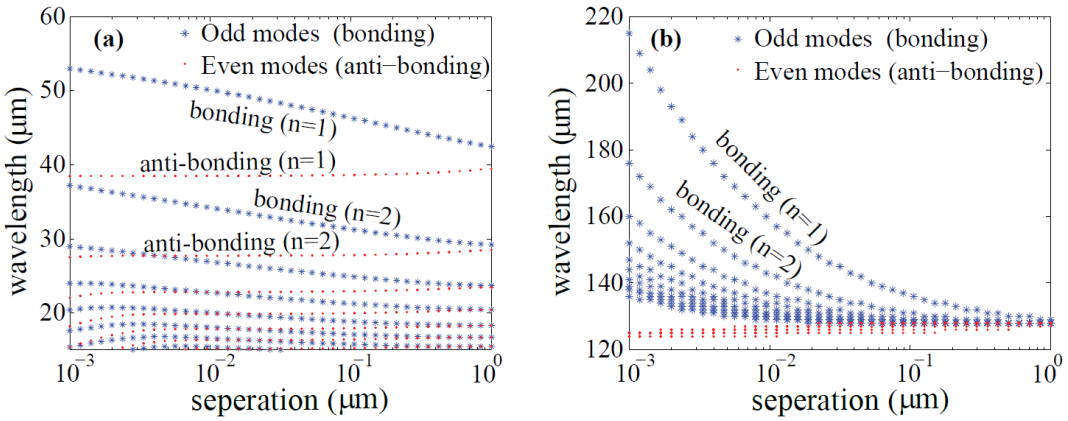

Figure.2-8 Mode distributions for (a) a graphene-coated dimer with glass as the core material (b) Indium antimonide dimer against different separations ($r_1 = r_2 = 1$ μm). Red dots are for the even anti-bonding modes and blue stars are for the odd bonding modes. Reprinted with permission from ref. [105] © 2017 Optical Society of America.

Figure.2-8 shows how the resonant frequencies of eigenmodes shift when varying the gap size between two nanowires with radius $r_1 = r_2 = 1$ μm in the configurations of (a) a glass-core-graphene shell dimer and (b) an InSb dimer without any shell. For the case where the shell is made of semiconductor of a certain thickness, its permittivity can be related to the conductivity by

$$\varepsilon = 1 + i\frac{\sigma'}{\omega\varepsilon_0\Delta d'} \tag{2.31}$$

We choose Indium antimonide (InSb) in our calculation as a counterpart to graphene for its small energy band gap and large electronic mobility [108]. The values of permittivity of InSb at THz frequencies are similar to those of metals in the visible and near infrared [109,110]. The complex permittivity of InSb can be modeled through a Drude-like formula $\varepsilon(\omega) = \varepsilon_\infty[1 - \omega_p^2/(\omega^2 + i\omega\gamma)]$ with parameters obtained by fitting experimental data ($\varepsilon_\infty = 15.68, \omega_p = 1.52 \times 10^{13}$ rad/s, $\gamma = 1.79 \times 10^{12}$ rad/s) [103].

In Fig.2-8, we plot the resonant frequencies for both $\hat{x}$ and $\hat{y}$ polarized illuminations. It can be clearly observed that the modes fall into two branches corresponding to two different polarized incident waves; the odd bonding modes ($\hat{x}$ polarized) denoted by blue stars and the even anti-bonding modes ($\hat{y}$ polarized) denoted by red dots. As shown in Fig.2-8 (a) and (b), for both structures the odd modes redshift as the nanowires approach each other, whereas the even modes blueshift as the gap reduces. This can be understood by the odd and even nature of modes with respect to the symmetry plane along the y direction, which is well illustrated in their field profiles (Fig.2-9). For the odd modes, as the nanowires approach each other, the attraction of opposite charges drags down the modes' frequencies. In contrast, for the even modes, the repulsion of like charges drives up the resonant frequencies as the gap is reduced.

Although the resonant frequency of dimers with and without a shell moves in a similar fashion when altering the gap size, they exhibit entirely different patterns. In Fig.2-8 (b), for InSb dimer without shell, when the gap is large and comparable to dimer's radius, all the modes are resonant at the vicinity of the surface plasma frequency $\boldsymbol{\omega_{sp}}$, which is similar to an individual nanowire. As the nanowires approach, more odd resonance modes of smaller orders (n) are excited and their frequencies are redshifted toward zero frequency when the gap decreases. While the odd modes spread out to form a continuous and broadband spectrum, the even modes, on the other hand, tend to the bulk plasma frequency $\boldsymbol{\omega_p}$ and are affected by the gap size only to a small extent compared to the odd modes. However, for the glass dimer coated graphene monolayer (Fig.2-8 (a)), branches of the even modes spread out and are paired with the odd modes instead of being constrained to frequencies between $\boldsymbol{\omega_{sp}}$ and $\boldsymbol{\omega_p}$, leading to a broadband response for both $\hat{x}$ and $\hat{y}$ polarized illumination. This is a major difference from conventional plasmonic dimers (without graphene shell) which obtain a broadband response only at certain polarization [103]. Furthermore, unlike the InSb dimer case where the odd bonding modes extend to zero frequency as the gap size decreases, for the glass-core-graphene shell dimer, odd and even modes saturate to a finite frequency when the gap size is decreased.

In order to gain more physical insights into the resonant features of the glass-core-graphene-shell dimer, we study the field distributions of eigenmodes. The structure considered here consists of two 1 μm-radius glass-core-graphene-shell nanowires separated by 0.1 μm. Figure.2-9 displays the potential distribution of dipole (m=1) and quadrupole modes (m=2) under $\hat{x}$ (upper panel) and $\hat{y}$ (lower panel) polarized incident waves in the physical and transformed spaces, respectively. The field profiles of the corresponding dark modes, which refers to non-radiative modes that

cannot couple directly with the incident plane wave, are also shown next to that of the radiative bright mode. From Fig.2-9 it can be seen that if the potential distribution in the real space is relatively smooth, in the transformed space it will become highly localized, and vice versa. Note that in the transformed annulus region, the left-hand side of the annulus is transformed to the gap while the right-hand side is mapped to infinity. Previous studies [89] showed that for an annulus comprised of homogenous materials, the mode is almost uniformly distributed. On the contrary, for the graphene case, the mode tends to stay on the right-hand side of the annulus. Correspondingly, in the physical space, the energy is well spread out, leading to the absence of strong hot spots.

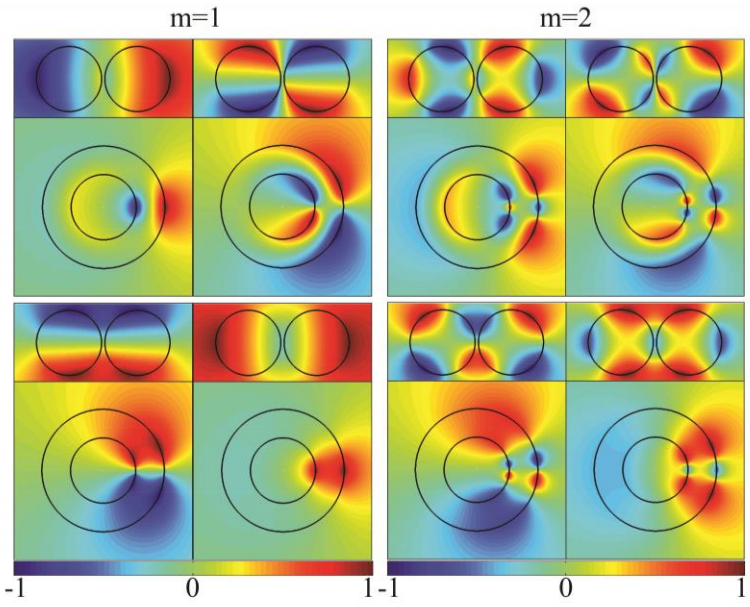

Figure.2-9 The potential distribution shown in real space and in the transformed space for glass-core-graphene-shell dimer ($r_1 = r_2 = 1$ μm, separation=0.1 μm). The mode order increase from left panel to right panel from dipole mode (m=1) to quadrupole mode (m=2). For each order, the corresponding dark eigenmode at the same frequency is also shown next to the bright mode. The upper panel corresponding to odd bonding modes, the lower panel is for even anti-bonding modes. Reprinted with permission from ref. [105] © 2017 Optical Society of America.

To further demonstrate the validity of our theory, in Fig.2-10 the calculated scattering and absorption spectra of the glass-core-shell dimer are compared with the results of numerical simulations (COMSOL Multiphysics). The graphene layer is modeled as a thin film with thickness Δd=1 nm, and the volumetric permittivity described by eq. 2.31 in COMSOL. Good agreement is observed when radius of nanowire is relatively small (1~2 μm). For larger structure dimensions, the theoretical predictions are slightly blueshifted compared to the numerical results. This is due to the phase retardation effects which are not considered in our approach [93] where the entire particle is assumed to experience the phase. Nevertheless, the magnitude and line shape of the spectra are still quantitatively predicted for nanowire radii up to 5 μm. Two Fano dips can be observed in the scattering spectra which are shifted towards longer wavelength as the radius increases. The dip at the longer wavelength results from the destructive interference between dipole (n=1) and quadrupole (n=2) modes that are resonant at each side of the dip supported by the dimer [84], which can be regarded as a bright mode and a dark mode which interfere to form the Fano resonance. On the other hand, the sharp invisibility dip located at the shorter wavelength can be attributed to the scattering cancellation of the dielectric core and monolayer graphene shell, similar to the plasmonic cloak and the mantle cloak operating at visible and RF frequencies respectively [49,111,112]. The emergences of these Fano dips can lead to huge field enhancement because energy can be harvested without radiating into the far field [22]. This suggests potential applications in sensitive micro spectroscopy and nonlinear devices.

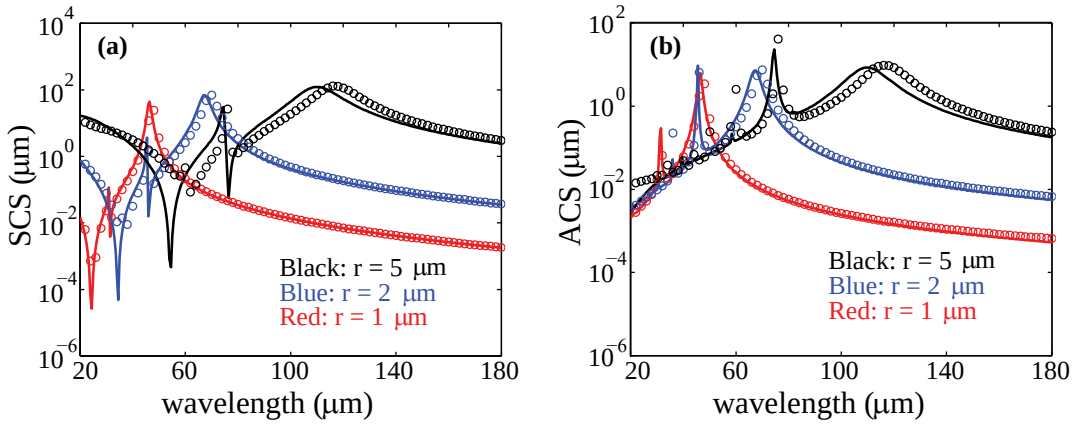

Figure.2-10 (a) Scattering and (b) absorption cross sections for glass-core-graphene-shell nanowires with different radius separated by 0.1 μm under $\hat{x}$ polarized illumination (odd bonding modes). Theory predictions (solid lines) are compared with simulations (circles). Reprinted with permission from ref. [105] © 2017 Optical Society of America.

In Fig.2-11, we investigate the electric field enhancement for dielectric-core-graphene-shell dimer (r = 1 μm) with different gap size and various core refractive index. Charge neutrality makes charges of the same magnitude and opposite sign piling up near the gap, which result in charge accumulation the small gap region, hence large field enhancement in between the gap can be observed. The field in the gap produced by these induced charges is inversely proportional to the gap distance (i.e., the same as in a capacitor), so it can be considerably enhanced with respect to the external field. From Fig.2-11 we can infer that although the graphene dimer shows poorer light focusing performance as compared with InSb dimer, the suppressed radiative behavior makes the field enhancement of the graphene dimer twice larger as compared with the InSb dimer.

Similar to conventional metallic nanoparticle dimers, for graphene coated nanowire dimer with narrow gap size down to a few angstroms, reduced plasmon field enhancement and broader resonance feature will be observed due to the nonlocality. In

addition, the plasmon enhancement is strongly influenced by the type of carbon edge terminations near the gap region. In particular, armchair edges produce larger induced fields and energy concentration than zigzag edges due to the additional losses introduced by zigzag edges [113].

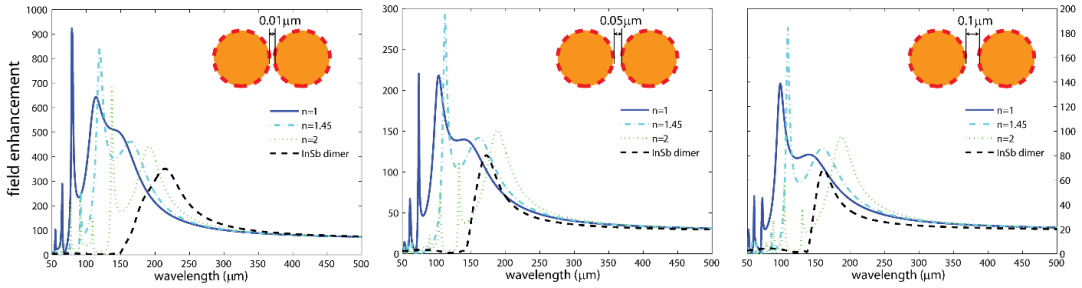

Figure.2-11 Electric field enhancement for dielectric-core-graphene-shell dimer (r=10μm) with different gap size (gap=0.01μm, 0.05μm, 0.1μm) and various core refractive index (n).

2.4 Conclusion

In conclusion, we have studied the plasmonic interactions between dielectric dimers coated with graphene monolayer using a modified transformation-optics approach. Comparison with simulation has shown that our theoretical model can predict the magnitude and line shape of the spectra for nanowire radii up to 5 μm. Our results show polarization independent broadband properties and multi-frequency Fano dips, contrary to conventional plasmonic dimer structures.

Chapter 3 Broadband negative refraction of highly squeezed hyperbolic polaritons in 2D materials

3.1 Background and motivation

Realizing negative refraction of highly squeezed polaritons, especially that supported by two-dimensional (2D) materials [31,33,35,62,114,115], such as graphene plasmon polaritons, largely facilitate the implementation of light manipulation at nanoscale [3,116,117], and can promise many photonic and optoelectronic applications [38,40,63,118-122]. In 2017, the phenomenon of negative refraction between extremely squeezed *isotropic* graphene plasmons and hexagonal boron nitride's (BN) phonon polaritons, with their in-plane polaritonic wavelengths squeezed by a factor over 100, is theoretically shown possible in graphene-BN heterostructures [56]. By following Ref. [56], the "squeezing factor" is defined as λ_0/λ_p, where λ_0 is the wavelength in the free space and λ_p is the wavelength of the surface polariton. On the other hand, the ultrahigh spatial confinement of these extremely squeezed isotropic polaritons also cause limitations on the manipulation of their dispersion relations [123]; in other words, their effective negative refractive index exists only within a certain frequency range. Consequently, the phenomenon of negative refraction of these extremely squeezed isotropic polaritons is restricted to happen only within a narrow frequency range (near 23 THz) with a bandwidth of less than 1 THz [56]. The narrow bandwidth unavoidably hinders the demonstration of this exotic phenomenon in experiments and thus the potential applications. It remains an open challenge to realize negative refraction effect of extremely squeezed polaritons within a broad frequency range.

Here we predict the phenomenon of broadband all-angle negative refraction of extremely squeezed *hyperbolic* polaritons, with their squeezing factor that can be over

100, in the infrared regime. The highly squeezed hyperbolic polaritons can be supported by nanostructured 2D materials such as graphene nanoribbon arrays [37,82] or BN nanoribbon arrays [79,124], by 2D materials supported by nanostructured substrates [40,80], or by naturally existing hyperbolic 2D materials such as black phosphorous [60,62]. In addition, we note that the hyperbolic polaritons can also be supported by metal based metasurfaces at visible [125,126] and even microwave [127] regimes. The peculiar isofrequency contour of hyperbolic polaritons [62,82,128] gives us an extra freedom to tailor their in-plane propagation direction, and thus the flexibility to realize the negative refraction effect of extremely squeezed polaritons in a wide frequency range. As an example, for the all-angle negative refraction of hyperbolic graphene plasmons shown below, the working bandwidth can vary from several tens of THz to over a hundred of THz by simply tuning the chemical potential of 2D materials. Our work indicates that 2D materials are a feasible platform for novel nanoimaging components, which is important for the manipulation light at extreme nanoscale.

We note that there are other types of negative refraction studied in the platform of 2D materials, including the negative refraction of electrons [129-131], negative refraction of light supported by a monolayer graphene [132], plasmonic [133,134] and optical [135,136] negative refraction in 3D bulk materials (i.e., 2D material-based periodic structures). However, these works mainly focused on the out of plane negative refraction effect with respect to the 2D materials, hence lacking the extreme in-plane spatial confinement of polaritons that is vital here. In addition, the all-angle negative refraction of graphene plasmons was studied in the hybrid graphene-photonic crystal structures [137], but the working bandwidth is still far less than 1 THz for a given chemical potential of graphene, along with the squeezing factor less than 20.

3.2 Dispersion of hybrid polaritons supported by anisotropic metasurfaces

To unveil the underlying physics, we begin with the studying of the dispersion of hyperbolic polaritons supported by a uniaxial metasurface. The metasurface can be modelled by an effective anisotropic surface conductivity of $\bar{\bar{\sigma}} = [\sigma_{xx}, \sigma_{yy}]$. Contrary to the isotropic metasurface (i.e. $\sigma_{xx} = \sigma_{yy}$) which supports the propagation of either transverse-magnetic (TM) [138,139] or transverse-electric (TE) polaritons [140-142], the anisotropic metasurface (i.e., $\sigma_{xx} \neq \sigma_{yy}$) supports the hybrid TM-TE polaritons [80,82,143-145]. Below we analytically solve the dispersion of these hybrid polaritons. We assume the anisotropic metasurface located at the interface (i.e., the plane of $z = 0$) between region 1 ($z > 0$, air) and region 2 ($z < 0$, substrate). To solve the eigenmode propagating along a direction having an angle φ with respect to the y axis, we define a new $x'y'z$ coordinates to be the original xyz coordinates rotated by an angle φ in the xy plane; this way, the eigenmode propagates exactly along the x' direction. In the following, we match the boundary conditions in the $x'y'z$ coordinates.

Within the frame of *k*DB system [104,138], the surface conductivity $\bar{\bar{\sigma}}'$ in the $x'y'z$ coordinates can be expressed as:

$$\bar{\bar{\sigma}}' = \bar{\bar{T}} \cdot \bar{\bar{\sigma}} \cdot \bar{\bar{T}}^{-1} = \begin{pmatrix} \sigma_{xx} sin\varphi^2 + \sigma_{yy} cos\varphi^2 & (\sigma_{xx} - \sigma_{yy}) sin\varphi cos\varphi & 0 \\ (\sigma_{xx} - \sigma_{yy}) sin\varphi cos\varphi & \sigma_{xx} cos\varphi^2 + \sigma_{yy} sin\varphi^2 & 0 \\ 0 & 0 & 0 \end{pmatrix} \quad (3.1)$$

where $\bar{\bar{T}} = \begin{pmatrix} sin\varphi & -cos\varphi & 0 \\ cos\varphi & sin\varphi & -sin\varphi \\ 0 & 0 & 1 \end{pmatrix}$, $\bar{\bar{T}} \cdot \bar{\bar{T}}^{-1} = \bar{\bar{I}}$ and $\bar{\bar{I}}$ is the unitary matrix.

For the hybrid TM-TE eigenmode, its total field can be written as the summation of field components of pure TM waves and field components of pure TE waves. Without loss of generality, a coefficient α is assumed for TE field components. Then we have

$$\bar{H}_{total} = \bar{H}_{TM} + \alpha \bar{H}_{TE} \tag{3.2}$$

$$\bar{E}_{total} = \bar{E}_{TM} + \alpha \bar{E}_{TE} \tag{3.3}$$

For TM waves, in the $x'y'z$ coordinates, the fields in each region can be expressed as

$$\bar{H}_{TM,1} = \hat{y}' e^{ik_{x'}x' + k_{z_1}z}$$

$$\bar{E}_{TM,1} = \frac{-1}{\omega \varepsilon_0 \varepsilon_{r1}} \left(k_{x'}\hat{z} + ik_{z_1}\hat{x}'\right) e^{ik_{x'}x' + k_{z_1}z} \tag{3.4}$$

$$\bar{H}_{TM,2} = \hat{y}' \cdot A e^{ik_{x'}x' - k_{z_2}z}$$

$$\bar{E}_{TM,2} = \frac{-1}{\omega \varepsilon_0 \varepsilon_{r2}} \bar{k}_2 \times \bar{H}_2 = \frac{-A}{\omega \varepsilon_0 \varepsilon_{r,2}} \left(\hat{z}k_{x'} - ik_{z_2}\hat{x}'\right) e^{ik_{x'}x' - k_{z_2}z}$$

For TE waves, in the $x'y'z$ coordinates, the fields in each region can be expressed as

$$\bar{E}_{TE,1} = \hat{y}' \alpha e^{ik_{x'}x' + k_{z_1}z}$$

$$\bar{H}_{TE,1} = \frac{\alpha}{\omega \mu_0} \left(k_{x'}\hat{z} + ik_{z_1}\hat{x}'\right) e^{ik_{x'}x' + k_{z_1}z} \tag{3.5}$$

$$\bar{E}_{TE,2} = \hat{y}' \cdot \alpha B e^{ik_{x'}x' - k_{z_2}z}$$

$$\bar{H}_{TE,2} = \frac{\alpha B}{\omega \mu_0} \left(k_{x'}\hat{z} - ik_{z_2}\hat{x}'\right) e^{ik_{x'}x' - k_{z_2}z}$$

In the above equations, $k_{z_j} = \sqrt{\frac{\omega^2}{c^2}\varepsilon_{rj} - k_{x'}^2 - k_{y'}^2}$ is the vertical wavevector component; ε_{rj} ($j = 1$ or 2) are the relative permittivities of regions 1 and 2, respectively; ω is the angular frequency; ε_0, μ_0 and c are the permittivity, permeability, and light speed in free space, respectively. The boundary conditions at $z = 0$ require $\hat{n} \times (\bar{E}_1 - \bar{E}_2) = 0$ and $\hat{n} \times (\bar{H}_1 - \bar{H}_2) = \bar{J}_s$, where $\hat{n} = -\hat{z}$. By solving the boundary conditions, we have

$$\left[1 + \frac{k_{z1}\varepsilon_{r2}}{k_{z2}\varepsilon_{r1}} + (\sigma_{xx}sin^2\varphi + \sigma_{yy}cos^2\varphi)\frac{k_{z1}}{\omega\varepsilon_0\varepsilon_{r1}}\right] = \frac{(\sigma_{xx} - \sigma_{yy})^2 sin^2\varphi cos^2\varphi \cdot \frac{ik_{z_1}}{\omega\varepsilon_0\varepsilon_{r1}}}{\sigma_{xx}cos^2\varphi + \sigma_{yy}sin^2\varphi + \frac{(k_{z1}+k_{z2})}{\omega\mu_0}} \tag{3.6}$$

where $sin^2\varphi = \frac{k_x^2}{k_x^2+k_y^2}, cos^2\varphi = \frac{k_y^2}{k_x^2+k_y^2}$. It is worthy to note that the left side of equation (3.6) is only relevant to the TM field components of hybrid polaritons, while the

denominator of the right side of equation (3.6) only corresponds to the TE field components. To some extent, the numerator of the right side of equation (3.6) denotes the coupling strength between TM and TE field components. For the extremely squeezed polaritons studied in this work, we show that equation (3.6) can be approximately reduced to

$$1+\frac{k_{z1}\varepsilon_{r2}}{k_{z2}\varepsilon_{r1}}+(\sigma_{xx}sin^2\varphi+\sigma_{yy}cos^2\varphi)\frac{k_{z1}}{\omega\varepsilon_0\varepsilon_{r1}}=0 \tag{3.7}$$

This is because $\left|\frac{(\sigma_{xx}-\sigma_{yy})^2 sin^2\varphi cos^2\varphi\cdot\frac{ik_{z1}}{\omega\varepsilon_0\varepsilon_{r1}}}{\sigma_{xx}cos^2\varphi+\sigma_{yy}sin^2\varphi+\frac{i(k_{z1}+k_{z2})}{\omega\mu_0}}\right| \approx \left|\frac{-(\sigma_{xx}-\sigma_{yy})^2\sin^2\phi\cos^2\phi}{\frac{2\varepsilon_0\varepsilon_{r1}}{\mu_0}}\right| \ll 1$ for extremely squeezed polaritons. Equations (3.6-7) indicate that the dispersion of hybrid TM-TE polaritons can be approximately governed by the dispersion of pure TM polaritons. The isofrequency contour governed by equation (3.7) is hyperbolic, when $Im(\sigma_{xx})\cdot Im(\sigma_{yy})<0$.

3.3 Results and discussion

3.3.1 Case 1: graphene ribbon arrays

As a conceptual demonstration, here in the first example we use the nanostructured graphene, i.e., graphene nanoribbon arrays, to create the hyperbolic metasurface; see the schematic structure in Fig.3-1 (a). According to Ref. [82], when the pitch L of nanoribbons is much smaller than the polaritonic wavelength $\lambda_{\text{polariton}}$, i.e., $L \ll \lambda_{\text{polariton}}$, the effective medium theory can be applied to describe the graphene metasurface. Then the effective anisotropic surface conductivity of graphene metasurface can be described by $\sigma_{xx,l}=\frac{L\sigma_s\sigma_C}{W\sigma_C+(L-W)\sigma_s}$ and $\sigma_{yy,l}=\sigma_s\frac{W}{L}$, where W is the width of nanoribbon, $\sigma_C=-i(\omega\varepsilon_0 L/\pi)\ln[\csc(\pi(L-W)/2L)]$ is an equivalent conductivity associated with the near-field couple between adjacent nanoribbons, and

σ_s is the surface conductivity of monolayer graphene modelled by the Kubo formula [82,146]:

$$\sigma_s = \frac{ie^2 k_B T}{\pi\hbar^2\left(\omega+\frac{i}{\tau}\right)}\left(\frac{\mu_c}{k_B T}+2\ln\left(e^{-\frac{\mu_c}{k_B T}}+1\right)\right)+\frac{ie^2(\omega+i/\tau)}{\pi\hbar^2}\int_0^{\infty}\frac{f_d(-x)-f_d(x)}{(\omega+i/\tau)^2-4(x/\hbar)^2}dx \qquad (3.8)$$

where $f_d(x) = (e^{(x-\mu_c)/k_B T}+1)^{-1}$ is the Fermi-Dirac distribution; k_B is the Boltzmann's constant; μ_c is the chemical potential; $T = 300$ K is the temperature; $\tau = \mu_c\mu/(ev_F^2)$ is the relaxation time; $v_F = 1\times10^6$ m/s is the Fermi velocity; e is the elementary charge. In this work, a conservative electron mobility of $\mu = 10000$ $cm^2V^{-1}s^{-1}$ (*36*, *37*) is adopted. Here the nanostructured graphene has a chemical potential of 0.1 eV, a conservative electron mobility of 10000 $cm^2V^{-1}s^{-1}$ [138,139], a pitch of $L = 30$ nm, and a width of $W = 20$ nm. Figure.3-1 (b) shows the hyperbolic isofrequency contour of extremely squeezed polaritons supported by graphene metasurface at 15 THz.

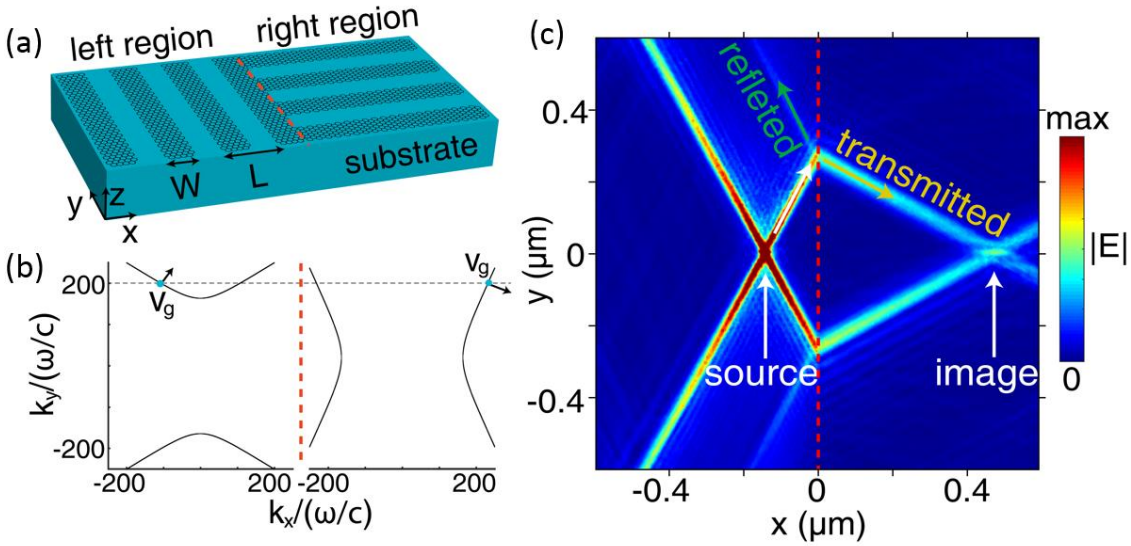

Figure.3-1 All-angle negative refraction of extremely squeezed polaritons supported by hyperbolic metasurfaces. (a) Structural schematic. The hyperbolic metasurfaces can be created by anisotropic 2D materials (such as black phosphorous) or nanostructured 2D materials (such as graphene nanoribbon array here). (b) Isofrequency contours of

hyperbolic graphene plasmons, supported by metasurfaces in left/right regions in (a). The dashed grey line represents the condition for conservation of wave vectors parallel to the boundary. The arrows represent the directions of group velocity, indicating that for polaritons in the left region incident with arbitrary angle, negative refraction can happen at the boundary. (c) Distribution of electric field $|\bar{E}|$ excited by a dipole source. The red dashed line represents the boundary between left/right regions. Here, and in the figures below, the nanostructured graphene has a conservative electron mobility of 10000 $cm^2V^{-1}s^{-1}$, a pitch of $L = 30$ nm, and a width of $W = 20$ nm. The chemical potential of graphene is 0.1 eV. The working frequency is 15 THz.

For the emergence of negative refraction phenomenon, the graphene metasurface in the right region in Fig.3-1 (a) shall be different from the left region. One simple way is to rotate the graphene metasurface in the right region with a certain angle with respect to the left region, such as 90^0 shown in Fig.3-1 (a). This way, the graphene metasurface in the right region can be characterized by a surface conductivity of $\bar{\bar{\sigma}}_r = [\sigma_{xx,r}, \sigma_{yy,r}]$, where $\sigma_{xx,r} = \sigma_{yy,l}$ and $\sigma_{yy,r} = \sigma_{xx,l}$. By applying the conservation law for wavevectors parallel to the boundary between left and right regions (i.e., parallel to $\hat{y}$), the y-component of group velocity for the incident hyperbolic polaritons in the left region is opposite to that for the transmitted hyperbolic polaritons in the right region, as shown in Fig.3-1 (b). This enables the negative refraction between hyperbolic polaritons in the left and right regions. In addition, we note that the hyperbolic polaritons in the left region can only propagate with a certain range of directions. Figure.1-3 (b) indicates that for these hyperbolic polaritons (i.e., incident from the left region with arbitrary angles), negative refraction can always happen at the boundary. By following Ref. [56,147,148], we also denote this phenomenon as the all-angle negative refraction of hyperbolic polaritons (i.e., graphene plasmons).

Figure.1-3 (c) numerically demonstrates the all-angle negative refraction of hyperbolic polaritons at 15 THz, by using the finite-element method (COMSOL Multiphysics). Hyperbolic polaritons are excited by a dipole source in the left region and propagate directionally towards the boundary. In experiment, polaritons in 2D materials are usually excited using small sources such as nanotip or quantum dots [79,149]. Here, we approximate the tip by a dipole source which will not affect the main conclusion. At the boundary, the polaritonic beams are negative refracted. Moreover, these beams converge to form an image in the right region, which computationally validates the all-angle negative refraction. Here the squeezing factor $\frac{Re(|\bar{k}_{||}|)}{\omega/c} > 100$ [see Fig.1-3 (b)] indicates that when compared with the wavelength in free space, the polaritonic wavelength is squeezed by a factor over 100. It is worthy to emphasize that the all-angle negative refraction of extremely squeezed hyperbolic polaritons with directional propagation, as an important advantage over that of isotropic polaritons which propagate omnidirectionally [56,147,148], might facilitate the design of novel compact guidance.

The FWHM (full width at half maximum) of the image for the point source shown in Fig.3-2 is only 0.035 μm, which is less than 1/100 of the working wavelength (i.e., 20 μm) in free space. This indicates that the extremely squeezed hyperbolic polaritons can enable deep-subwavelength imaging. We note that the imaging mechanism here is not a perfect image recovery, and some oscillations can be observed. This is because the reflection at the boundary is unavoidable due to impedance mismatch between the two hyperbolic metasurfaces, and the propagation loss of hyperbolic polaritons will degrade the imaging quality. Also, the light beam may experience multiple reflections from edges of the metasurfaces. To optimize the quality of formed image in the right region, one shall consider both reflection and the

propagation loss of polaritons [56,147,148].

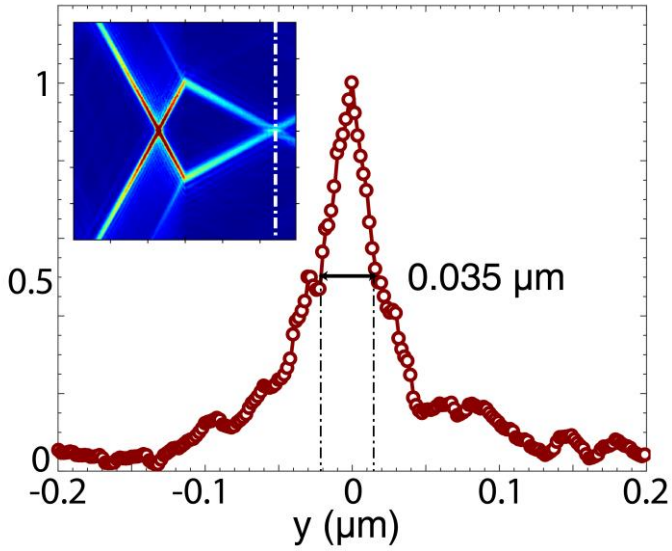

Figure.3-2 Full width at half maximum of the image for the point source in Fig.3-1 (c). The plotted electric field is along a line crossing the center of the image for the point source in Fig.3-1 (c); see the dashed line in the inset.

Figure.3-3 shows the effective anisotropic conductivity of graphene metasurface, which can help to infer the working frequency range of the all-angle negative refraction of hyperbolic polaritons. As shown in Fig.3-3 (a), the frequency range, that has $Im(\sigma_{xx,l}) \cdot Im(\sigma_{yy,l}) < 0$ and thus supports the hyperbolic polaritons, spans from 0 to 48 THz, when the chemical potential of graphene is 0.1 eV. It shall be noted that the phenomenon of all-angle negative refraction of hyperbolic polaritons can happen at arbitrary frequency within this frequency range, as long as the effective medium theory for graphene metasurface is valid (i.e., when $L \ll \lambda_{\text{polariton}}$).

To guarantee the validity of the effective medium theory for metasurfaces based on 2D materials, a small value of pitch L, which although might increase the complexity in structural fabrication [79,124], can be adopted. This way, the working bandwidth for the all-angle negative refraction of hyperbolic polaritons demonstrated here is not limited by the frequency range supporting negative-index polaritons (such

as in Ref. [56]). Consequently, the working bandwidth can be broadband and actively tunable via altering the chemical potential of 2D materials. Figure.3-3 (b) shows the working bandwidth of the negative refraction effect in graphene metasurfaces. The bandwidth of graphene metasurface having $Im(\sigma_{xx,l}) \cdot Im(\sigma_{yy,l}) < 0$ changes from 40 THz to over 100 THz, by increasing the chemical potential from 0.1 eV to 0.5 eV. Therefore, in principle, the bandwidth of all-angle negative refraction of hyperbolic polaritons can vary from several tens of THz to even over a hundred THz, by simply increasing the chemical potential of graphene.

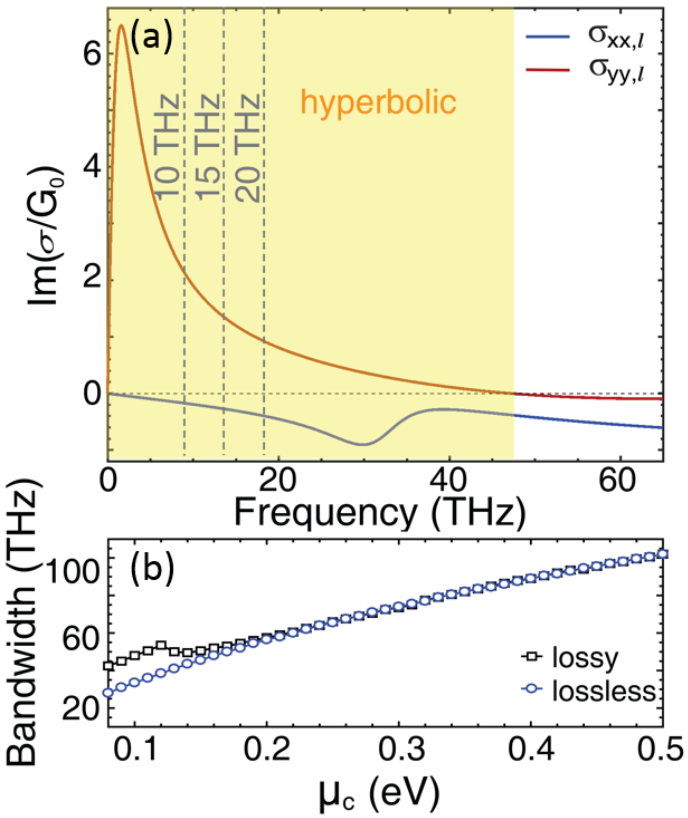

Figure.3-3 Broadband all-angle negative refraction of hyperbolic polaritons. (a) Imaginary part of surface conductivity of graphene metasurface, created by nanostructured graphene as shown in the left region of Fig.3-1 (a) and having an effective anisotropic surface conductivity of $\bar{\bar{\sigma}}_l = [\sigma_{xx,l}, \sigma_{yy,l}]$. The graphene metasurface supports hyperbolic plasmon polaritons when $Im(\sigma_{xx,l}) \cdot Im(\sigma_{yy,l}) < 0$,

i.e., the region highlighted by yellow. The chemical potential of graphene is $\mu_c =$ 0.1 eV. (b) Bandwidth of graphene metasurface having $Im(\sigma_{xx,l}) \cdot Im(\sigma_{yy,l}) < 0$, as a function of the chemical potential. The phenomenon of all-angle negative refraction of hyperbolic polaritons can happen within this bandwidth. The constant $G_0 = e^2/4\hbar$ is the universal optical surface conductivity.

Also, the real parts of the effective surface conductivity of graphene metasurface are shown in Fig.3-4. We note that $Re(\sigma_{yy,l}) \gg Re(\sigma_{xx,l})$ and $Re(\sigma_{xx,l}) \ll G_0$.

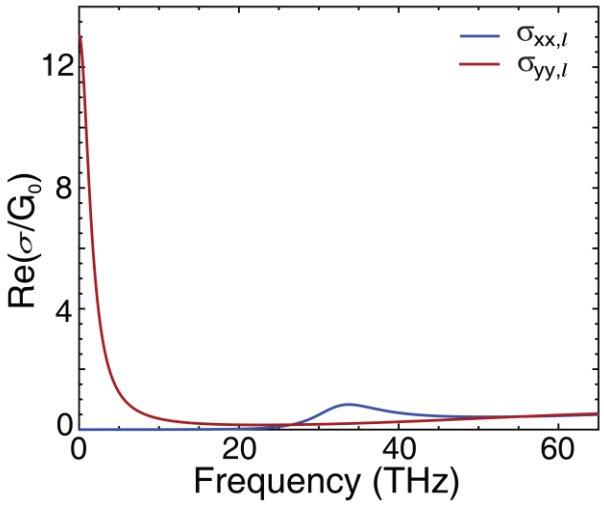

Figure.3-4 Real part of effective surface conductivity of graphene metasurface. The setup of graphene metasurface is the same as that in Fig.3-3 (a).

Interestingly, as illustrated in Fig.3-3 (b), the material loss can increase the bandwidth having $Im(\sigma_{xx,l}) \cdot Im(\sigma_{yy,l}) < 0$ when μ_c is smaller than 0.18 eV. Figure.3-5 shows that this is mainly due to the material loss has a strong influence on the sign of value of $Im(\sigma_{xx,l})$. When μ_c is large, such as $\mu_c = 0.2$ eV in Fig.3-5 (a), the bandwidth having $Im(\sigma_{xx,l}) \cdot Im(\sigma_{yy,l}) < 0$ is merely determined by the frequency where the sign of value of $Im(\sigma_{xx,l})$ changes from negative to positive.

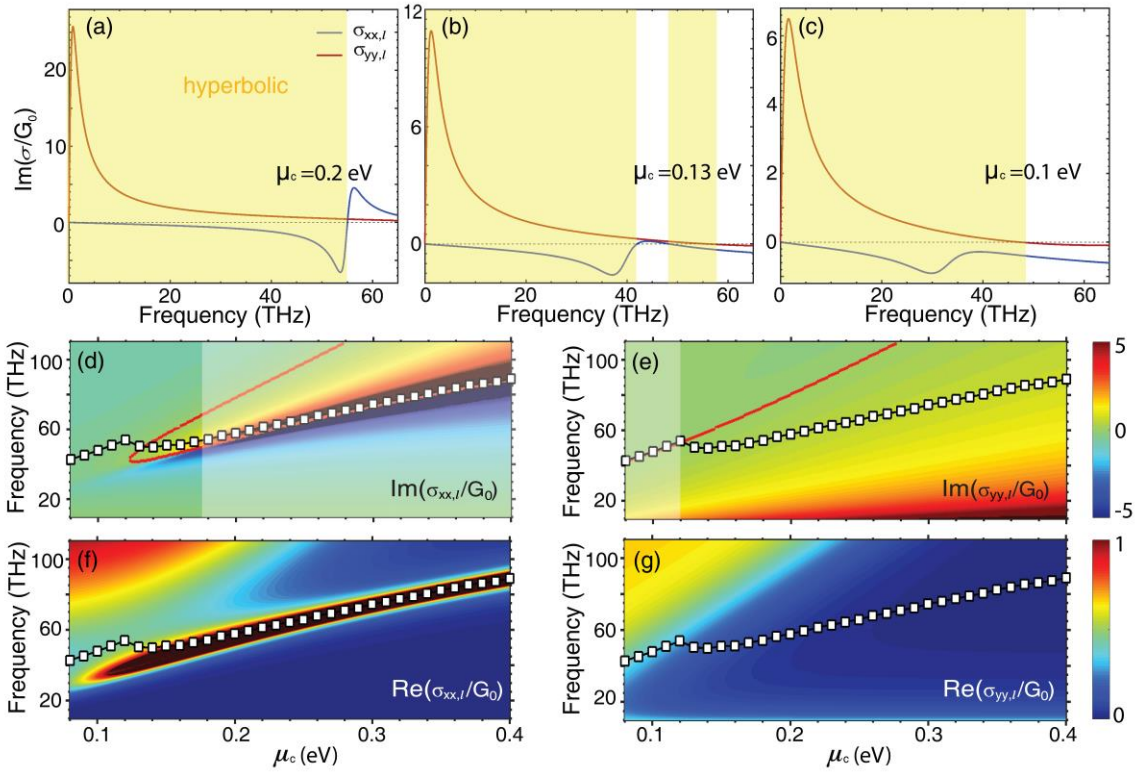

Figure.3-5 Loss influence on the bandwidth having $Im(\sigma_{xx,l}) \cdot Im(\sigma_{yy,l}) < 0$. (a-c) Effective surface conductivity of graphene metasurface at different chemical potentials. The region having $Im(\sigma_{xx,l}) \cdot Im(\sigma_{yy,l}) < 0$ is highlighted by light yellow. (d-g) Effective surface conductivity of graphene metasurface as a function of the chemical potential μ_c and the frequency. All other parameter setup is the same as Fig.3-3 (a). The red lines in (d, e) indicate that the value of $Im(\sigma_{xx,l})$ or $Im(\sigma_{yy,l})$ is zero. The line with square symbol is the same as the line of bandwidth having $Im(\sigma_{xx,l}) \cdot Im(\sigma_{yy,l}) < 0$ as a function of μ_c in Fig.3-3 (b). (d, e) show that the bandwidth having $Im(\sigma_{xx,l}) \cdot Im(\sigma_{yy,l}) < 0$ is determined by the frequency having $Im(\sigma_{xx,l}) = 0$ when $\mu_c > 0.2$ eV, and becomes determined by the frequency having $Im(\sigma_{yy,l}) = 0$ when $\mu_c < 0.12$ eV.

When μ_c decreases to a value near 0.18 eV, such as $\mu_c = 0.13$ eV in Fig.3-5 (b), there will be two separate frequency ranges having $Im(\sigma_{xx}) \cdot Im(\sigma_{yy}) < 0$. This

way, the bandwidth having $Im(\sigma_{xx,l}) \cdot Im(\sigma_{yy,l}) < 0$ is determined simultaneously by the frequency where the sign of value of $Im(\sigma_{xx,l})$ changes from negative to positive and the frequency where the sign of value of $Im(\sigma_{xx,l})$ changes from positive to negative. It is the appearance of the additional frequency range having $Im(\sigma_{xx,l}) \cdot Im(\sigma_{yy,l}) < 0$ that increases the total bandwidth having $Im(\sigma_{xx,l}) \cdot Im(\sigma_{yy,l}) < 0$. When μ_c further decreases, such as $\mu_c = 0.10$ eV in Fig.3-5 (c), the value of $Im(\sigma_{xx,l})$ is always negative in the interested frequency range; this way, the bandwidth having $Im(\sigma_{xx,l}) \cdot Im(\sigma_{yy,l}) < 0$ becomes to be determined by the frequency where the sign of value of $Im(\sigma_{yy,l})$ changes from positive to negative. As a summary, we plot the values of $\sigma_{xx,l}$ and $\sigma_{yy,l}$ as a function of μ_c and frequency in Fig.3-5 (d-g). The results in Fig.3-5 (d-g) is in accordance with the analysis in Fig.3-5 (a-c). In addition, the relative bandwidth for negative refraction of hyperbolic polaritons can be up to 2, if we define the relative bandwidth as $\frac{f_{\max}-f_{\min}}{(f_{\max}+f_{\min})/2}$, where $f_{\max}$ and $f_{\min}$ ($f_{\min} \to 0$) are the maximum and minimum frequencies supporting the negative refraction of hyperbolic polaritons.

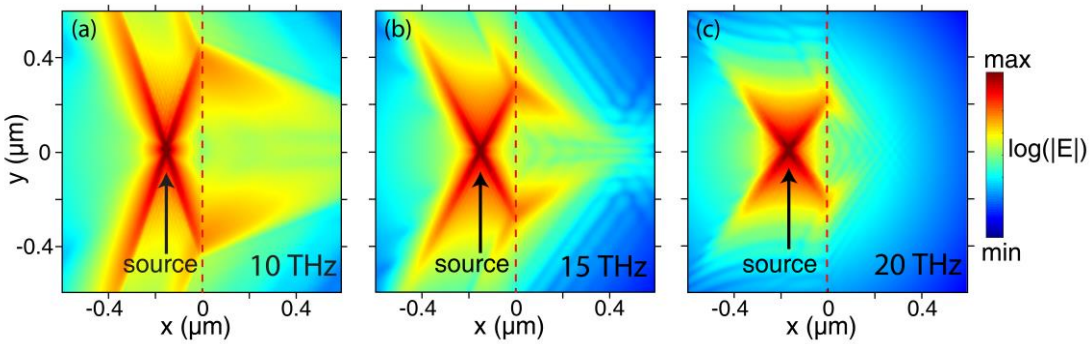

Figure.3-6 All-angle negative refraction of hyperbolic polaritons when the real material loss is considered. The working frequency is (a) 10 THz, (b) 15 THz and (c) 20 THz, respectively. The other parameters are the same as that in Fig.3-1 (c).

To get a vivid understanding of the loss influence, we show the phenomenon of

all-angle negative refraction with the consideration of realistic material loss in Fig.3-6. The material loss will degrade the propagation length of the hyperbolic graphene plasmons and thus the performance of all-angle negative refraction.

In addition, the isofrequency contours of hyperbolic graphene plasmons, supported by metasurfaces in the left region in Fig.3-1 (a), are shown in Figure.3-7 for different frequencies. We can see from Figure.3-7 that the squeezing factor $k_\rho/(\omega/c) = \sqrt{k_x^2 + k_y^2}/(\omega/c)$ is larger than 100 at the studied frequency range. Since the negative refraction of graphene plasmons in this work is enabled by the hyperbolic isofrequency contour of graphene plasmons, which exists below 48 THz for the case in Fig.3-3 (a) (see the hyperbolic isofrequency contours at 1 THz and 40 THz in Fig.3-7 for example), it is reasonable to argue that the negative refraction of hyperbolic polaritons exists below 48 THz for the case in Fig.3-3 (a).

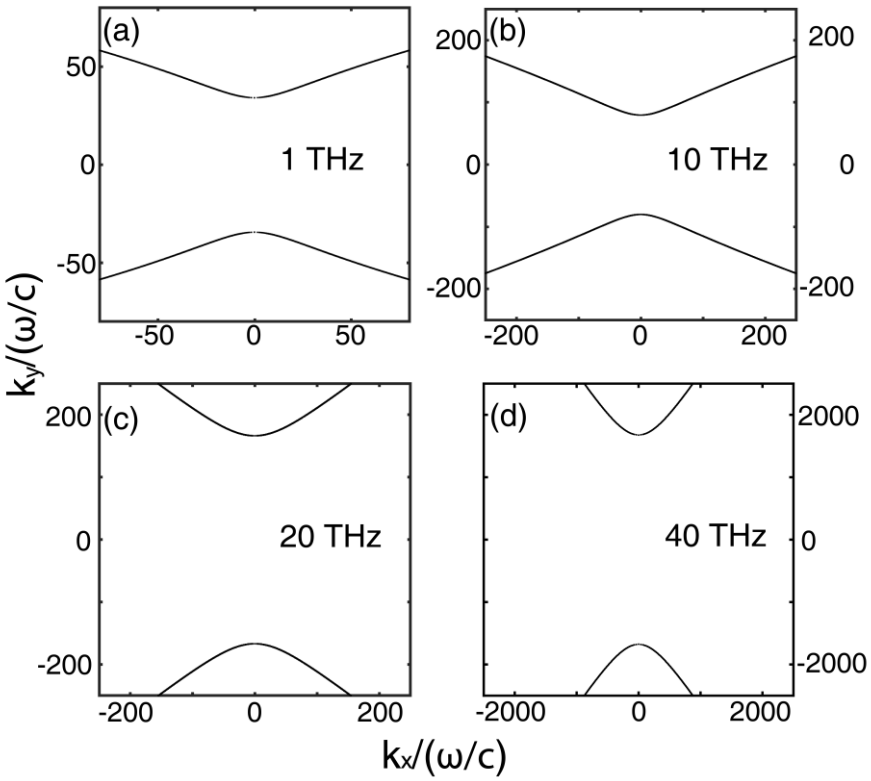

Figure.3-7 Isofrequency contours of hyperbolic graphene plasmons at 1 THz and 40 THz. The working frequencies are (a) 1 THz, (b) 10 THz, (c) 20 THz and (d) 40 THz respectively. All parameter setups are the same as Fig.3-1 (b).

To numerically validate the all-angle negative refraction of hyperbolic polaritons in a broad frequency range, Fig.3-8 demonstrates this phenomenon at other frequencies, i.e., at 10 THz in Fig.3-8 (a) and at 20 THz in Fig.3-8 (b). The squeezing factors for hyperbolic polaritons at these two frequencies are both over 100 (see Fig.3-7 (b)&(c)). Therefore, by using hyperbolic metasurfaces based on 2D materials, we can extend the working bandwidth of all-angle negative refraction of extremely squeezed polaritons to at least several tens of THz, which is favored for practical applications.

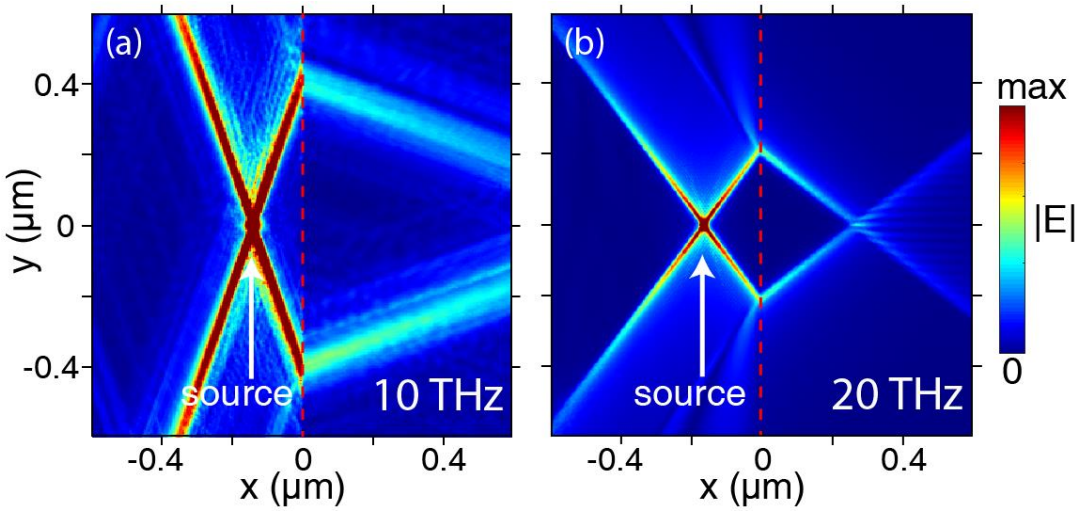

Figure.3-8 All-angle negative refraction of hyperbolic polaritons (a) at 10 THz and (b) at 20 THz. The other parameters are the same as that in Fig.3-1 (c). The value of anisotropic surface conductivity for graphene metasurfaces are highlighted by grey dashed lines in Fig.3-3 (a).

Finally, Fig.3-9 below shows that the change of the permittivity of substrate has small influence on the performance of the all-angle negative refraction of hyperbolic graphene plasmons. The main conclusions of this work should equally apply to graphene metasurfaces supported by a wide range of different substrates. This gives us the flexibility in choosing the substrate materials. In this work, the dielectric with a relative permittivity of 3.6 (e.g. SiO_2) is chosen as the substrate for conceptual

demonstration. For clarity of conceptual demonstration, the substrate loss is assumed to be transparent. In this work, the simulation was done in 3D, and the pattern on the image side is due to the interference of multiple reflected light beams.

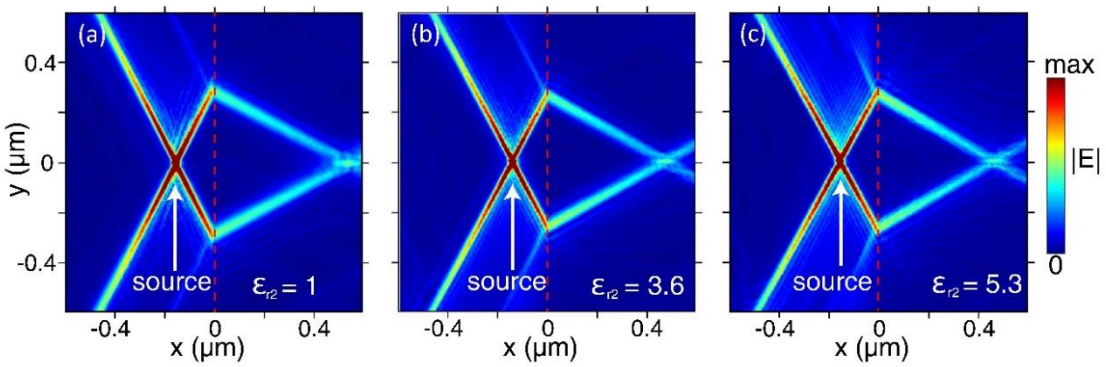

Figure.3-9 Substrate influence on the all-angle negative refraction of hyperbolic graphene plasmons at 15 THz. The value of relative permittivity of the substrate is 1 in (a), 3.6 in (b) and 5.3 in (c), respectively. All other parameter setup is the same as Fig.3-1 (c) and Fig.3-8.

3.3.2 Case 2: natural anisotropic 2D materials

To further extend the bandwidth of all-angle negative refraction of extremely squeezed polaritons, one may adopt the naturally anisotropic 2D materials to support tunable hyperbolic polaritons, such as those described in Ref. [62] including black phosphorous. From Ref. [62], these 2D materials can be directly characterized by an anisotropic surface conductivity, i.e.,

$$\sigma_{jj} = \frac{ie^2}{\omega + i/\tau} \cdot \frac{n}{m_j} + s_j \left[\Theta(\omega - \omega_j) + \frac{i}{\pi}\right], j = x, y \tag{3.9}$$

where n is the concentration of electrons, m_j is the electron's effective mass along the j direction, τ is the relaxation time, ω_j is the frequency of the onset of interband transitions for the j component of conductivity, s_j accounts for the strength of interband component, and $\Theta(\omega - \omega_j)$ is a step function. Equation (3.9) circumvents the requirement (i.e., $L \ll \lambda_{\text{polariton}}$ discussed in the above) for the validity of effective

medium theory for metasurfaces based on nanostructured 2D materials. For these anisotropic 2D materials, the value of n can be flexibly tunable via electrostatic gating, just like graphene, and ω_x can be different from ω_y. These, along with the broad class of anisotropic materials, give us the flexibility to realize the negative refraction effect of extremely squeezed polaritons in a broad frequency range.

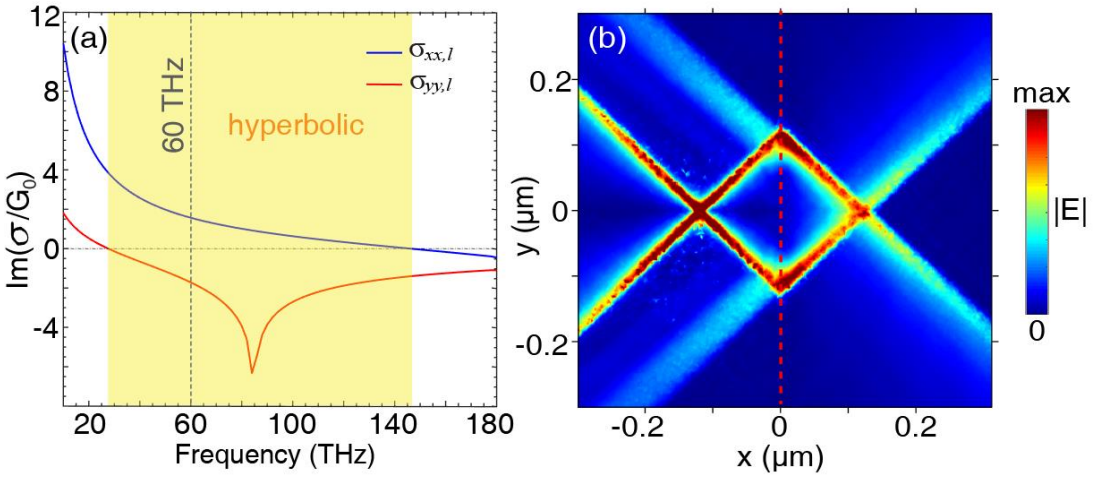

Figure.3-10 Negative refraction of hyperbolic polaritons supported by naturally anisotropic 2D materials. (a) Imaginary part of surface conductivity of anisotropic 2D material in the left region. In equation (3.9), we set $n = 3 \times 10^{13}\ cm^{-2}$, $m_x = 0.2m_0$, $m_y = m_0$, $\omega_x = 1$ eV, $\omega_y = 0.35$ eV, $\tau = 0.4$ ps, $s_x = 1.7s_0$ and $s_y = 3.7s_0$, where $s_0 = e^2/4\hbar$ and m_0 is the free-electron mass. (b) Distribution of electric field $|\bar{E}|$ excited by a dipole source at 60 THz. The red dashed line represents the boundary between left/right regions. For the right region, we have $\sigma_{xx,r} = \sigma_{yy,l}$ and $\sigma_{yy,r} = \sigma_{xx,l}$.

As a concrete example, Fig.3-10 shows the all-angle negative refraction of hyperbolic polaritons supported by the naturally anisotropic 2D materials. By following Ref. [62], here we set $n = 3 \times 10^{13}\ cm^{-2}$, $m_x = 0.2m_0$, $m_y = m_0$, $\omega_x = 1$ eV, $\omega_y = 0.35$ eV, $\tau = 0.4$ ps, $s_x = 1.7s_0$ and $s_y = 3.7s_0$, where $s_0 = e^2/4\hbar$ and m_0 is the free-electron mass. The frequency range, that has $Im(\sigma_{xx,l}) \cdot Im(\sigma_{yy,l}) < 0$

and thus supports the hyperbolic polaritons, spans from 24 to 143 THz in Fig.3-10 (a), with a bandwidth of 119 THz. This indicates that the negative refraction of hyperbolic polaritons exist within the above frequency range; see the negative refraction of hyperbolic polaritons at 60 THz in Fig.3-10 (b) for example.

3.4 Conclusion

In conclusion, we have revealed a feasible way to realize negative refraction of extremely squeezed polariton in a broadband infrared regime, by utilizing hyperbolic metasurfaces based on 2D materials or naturally anisotropic 2D materials. Due to the combined advantages of highly directional propagation, active tunability, low loss and ultrahigh confinement provided by hyperbolic polaritons in 2D materials, the broad class of 2D materials can provide a versatile platform for the manipulation of light-matter interaction at the extreme nanoscale and for the design of highly compact nano-devices and circuits.

Chapter 4 Unidirectional waveguiding based on drift-induced nonreciprocal graphene

4.1 Background and motivation

Nonreciprocal systems refer to systems breaking the symmetry of Lorentz reciprocity where the response remains unchanged when altering the propagation direction of light. Conventionally, magneto-optical effects of surface plasmons of thin metal or 2D materials are exploited to break the Lorentz reciprocity, in analogous to the chiral edge states stems from the quantum Hall effect of electrons [150]. For example, in Ref. [151] and Ref. [152] multiport waveguide/isolators designs with tunable directionality are demonstrated, making use of the electromagnetic nonreciprocal and gyrotropic properties of magnetically biased graphene. However, this method relies strongly on large magnetic fields and bulky magnetic materials that opposing the trends of miniaturization for modern devices. Therefore, alternative methods arise to achieve nonreciprocity without external magnetic field, including spatiotemporal modulation [153] and nonlinear materials [154].

Recently, graphene monolayer electrically biased with drift current is demonstrated to support robust unidirectional propagation immune to back-scattering from obstacles [155], taking advantage of the extremely high electron mobility of graphene that enables large drift velocity not possible for typical metals and semiconductors. Drift velocities on the order of the Fermi velocity ($v_F \approx c/300$) have been experimentally reported in suspended graphene samples [156], graphene encapsulated in hexagonal boron nitride [157] and graphene samples under rapid electrical pulsing [158]. In this work, we adopt this property to design a three-port waveguide based on double layer nonreciprocal graphene biased with drift current. Firstly, the dispersion relations and field distributions of double- and single-layer

nonreciprocal graphene will be investigated, and then we will verify the directional propagation of the three-port waveguide under study. The compatible directional guiding demonstrated in this work made possible by nonreciprocal graphene plasmons is appealing for applications such as directional coupler, circulator and isolator that blocks unwanted reflections, which are fundamental building blocks of optical communications systems and photonic circuitry.

4.2 Drift-induced unidirectional surface plasmons in graphene

4.2.1 Single layer biased graphene

First, we start by investigating the SPP dispersion relation of single layer and double layer graphene biased with drift electric current, to build a solid theoretic foundation for the design of the nonreciprocal waveguide in the next part.

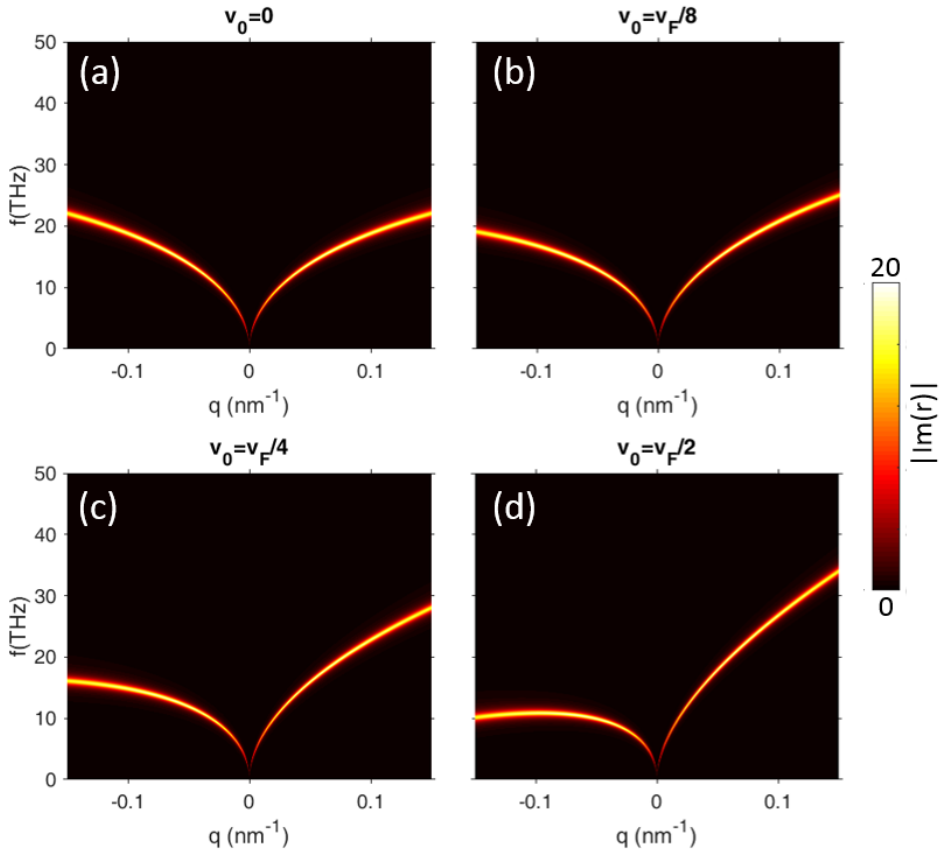

Figure.4-1 Dispersion of graphene SPP (by plotting the absolute value of the imaginary part of the Fresnel reflection coefficient) with different values of v_0 spans from (a)

$v_0 = 0$, (b) $v_0 = v_F/8$, (c) $v_0 = v_F/4$ to (d) $v_0 = v_F/2$. $v_F = 10^6\ m/s$ is the Fermi velocity.

Here the graphene monolayer is embedded in SiO_2 with $\varepsilon_s = 4$, and the surface conductivity $\sigma_s(\omega)$ follows the Kubo formula (see eq. 2.8 and 2.9 in chapter 2) consisting of the intraband and interband contributions. The temperature T = 300 K, chemical potential $\mu_c = 0.1$ eV, and the intraband and interband phenomenological relaxation time τ_{intra} and τ_{inter} are 0.35 ps and 0.0658 ps [159], respectively. In Ref. [47] T. A. Morgado et al. proposed that the surface conductivity of graphene electrically biased along the longitudinal direction can be effectively described as $\sigma_s^{drift}(\omega, q) = (\omega/\widetilde{\omega})\sigma_s(\widetilde{\omega})$, where q is the wavevector component along the x axis and $\widetilde{\omega} = \omega - qv_0$ is the shifted frequency. Hence, we can infer from this expression that the graphene layer acquires a nonreciprocal response since negative and positive q will result in different conductivity for nonzero v_0 (i.e. for $v_0 \neq 0$, $\sigma_s^{drift}(\omega, q) \neq \sigma_s^{drift}(\omega, -q)$). The dispersion diagrams shown in Fig.4-1 (b-d) give concrete evidence of this argument through the asymmetric SPP dispersion curves along the positive and negative direction of the x axis with a nonzero v_0. Also, note that taking account of the nonlocal effects (not considered here) of graphene reduces the nonreciprocal effects but the drift-induced SPP will retain its properties of asymmetry and directionality [155].

To gain more physical insight into the unidirectional propagation property of drift-induced graphene plasmon, next in Figure.4-2 we plot the $\hat{x}$ component of the electric field excited by a source linearly polarized in the $\hat{z}$ direction 10 nm above the graphene layer. Analytical solution of the field distribution can be obtained by expanding all the fields including the cylindrical wave radiated by the emitter, the

reflected and transmitted wave into plane wave terms, and then match the corresponding modes via imposing the boundary conditions at z = 0. As illustrated in Fig.4-2 (b), the field patterns are in agreement with the dispersion diagram in Fig.4-2 (a). The electric field pattern at 20 THz (upper panel of Fig.4-2 (b)) behave completely different form the rest two frequencies, which exhibits one-way propagation along the $+\hat{x}$ direction. The dispersion relation in Fig.4-2 (a) implies that the reason for this behavior can be attribute to the asymmetric response for negative and positive q under DC (direct current) biasing, which leads to a unidirectional propagation band for frequencies above 16.3 THz, where only propagation along the $+\hat{x}$ direction is allowed. The solution for negative q (not shown in the figure) represents strongly attenuated waves with large imaginary parts of the wavenumbers. Therefore, the SPP propagation along the $-\hat{x}$ direction is forbidden (highly attenuated). Moreover, due to the nonreciprocal response, the wavelength and propagation length are also distinct for the $-\hat{x}$ and $+\hat{x}$ directions. For example, at f = 15 THz shown in the middle panel of Fig.4-2 (b), SPP mode in the left half region has a shorter wavelength and a wavenumber ($q = -0.1\ nm^{-1}$) that is twice larger in magnitude than that of the right region ($q = 0.04\ nm^{-1}$).

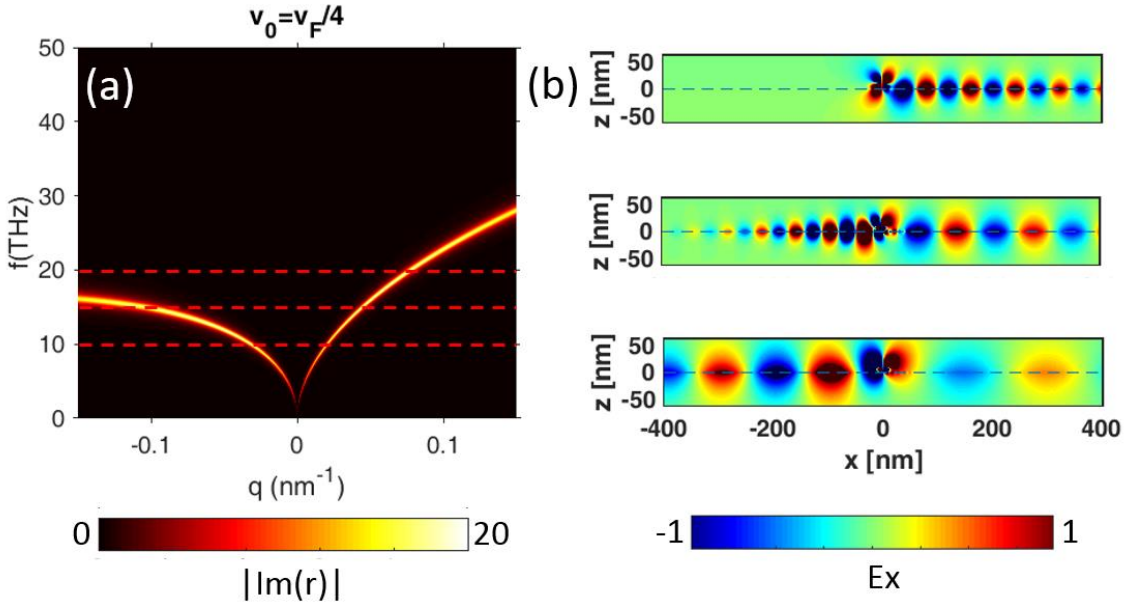

Figure.4-2 (a) Dispersion of graphene SPP when the drift velocity $v_0 = v_F/4$. (b) Electric field distribution E_x excited by an emitter polarized in the $\hat{z}$ direction placed at 10 nm above the graphene sheet (the horizontal blue dashed line). Upper: frequency f = 20 THz; middle: f = 15 THz; lower: f = 10 THz, corresponding to the three horizontal red dashed lines in (a).

4.2.2 Double layer biased graphene

Next, we proceed to examine the case of double graphene layers with nonreciprocity in close vicinity. Here we consider two graphene sheets biased with opposite drift current separated by a gap of size d = 10 nm, and the surrounding medium is SiO_2 with $\varepsilon_s = 4$. As shown in Fig.4-3, a pair of hybridized modes can be observed in the dispersion diagram of double layer graphene biased oppositely. As the drift velocity v_0 increases, the two hybridized modes repel each other in terms of mode frequency, and the mode with lower energy and positive q becomes weaker compared to other modes.

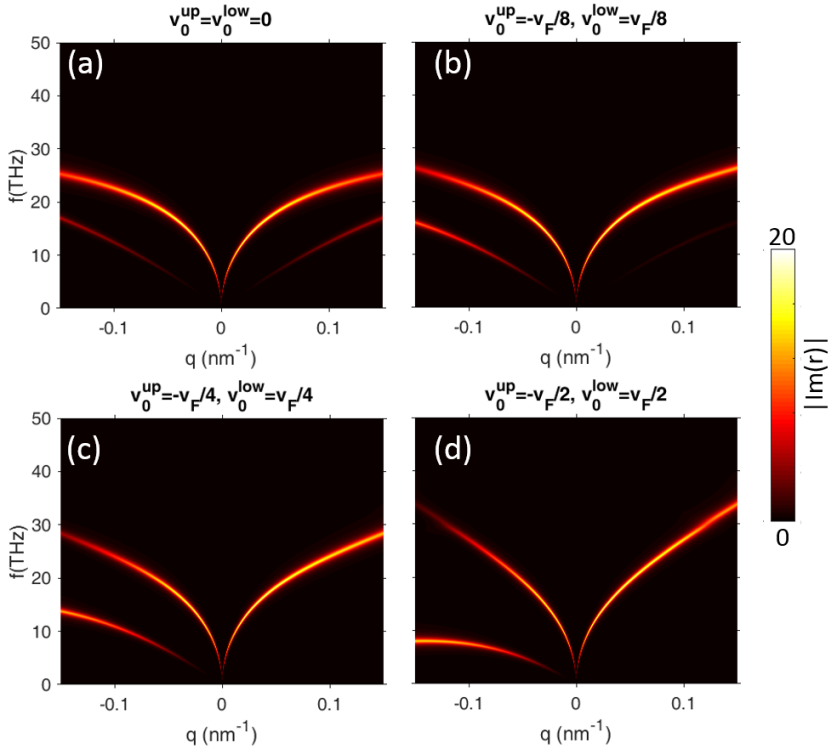

Figure.4-3 Dispersion of SPP in two graphene layers (by plotting the absolute value of

the imaginary part of the reflection coefficient) with different values of v_0 from (a) $v_0 = 0$, (b) $v_0 = v_F/8$, (c) $v_0 = v_F/4$ to (d) $v_0 = v_F/2$. $v_F = 10^6\ m/s$ is the Fermi velocity.

Also, as illustrated in Fig.4-4 (b), the wavelength of the double layer graphene SPP at 20 THz (corresponding to the red dashed line in Fig.4-4 (a)) is consistent with the intersection point with the branch with positive q in the right region.

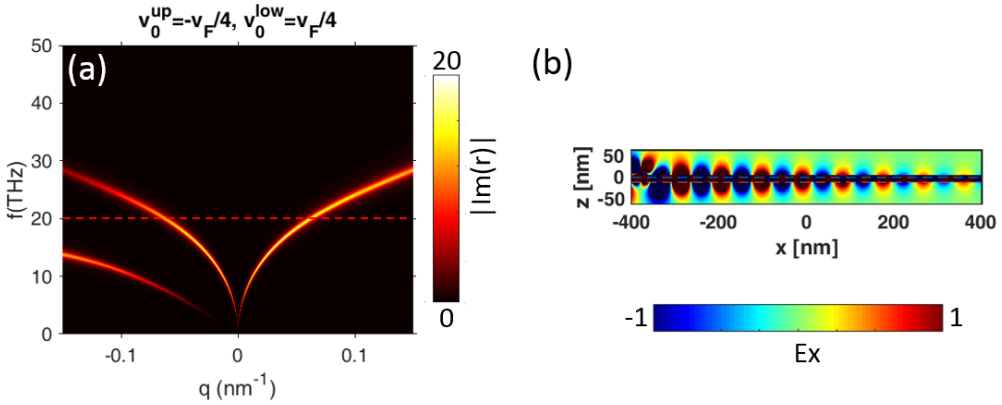

Figure.4-4 (a) Dispersion of double layer graphene SPP when the drift velocity for the upper layer $v_0^{up} = -v_F/4$ and for the lower layer $v_0^{low} = v_F/4$. The gap size d is 10 nm. (b) Electric field distribution E_x excited by an emitter polarized in the $\hat{z}$ direction placed at 10 nm above the upper graphene sheet (emitter's coordinates: $x_0 = -380\ nm, z_0 = 10\ nm$).

4.3 Results and discussion

Figure.4-5 illustrate a Y-shaped waveguide based on the drift induced nonreciprocal graphene layer under study. The upper layer and lower graphene are biased with opposite drift current ($v_0^{up} = -v_F/4$, $v_0^{low} = v_F/4$), and the operation frequency is chosen to be 20 THz, within the unidirectional band shown in Fig.4-2. The left part of the waveguide is a dielectric/graphene/dielectric/graphene interface with gap size equal to 10 nm, and the dielectric here is SiO_2 with $\varepsilon_s = 4$, while in the right

part two graphene sheets forms two separate dielectric/graphene/dielectric interfaces. The graphene layer here has relaxation time $\tau = 1$ ps, $\mu_c = 0.1$ eV, T = 300 k. Note that minor difference in the level of loss of graphene (relaxation time τ) will not affect the line shape of the calculated dispersion curves. An electric point dipole is placed 10 nm above the upper layer graphene of the left part to excite the SPP.

The numerical simulated field distribution clearly displayed the directional propagation property of the Y-shaped waveguide based on oppositely biased graphene (Fig.4-5 (b)), where the SPP propagation along the $+\hat{x}$ direction is forbidden in the upper branch. This is consistent with the analysis in Fig.4-2 but here the asymmetric dispersion curve is inverted in the $\hat{x}$ axis, resulting in a forbidden band above 16.3 THz for the $+\hat{x}$ direction. Moreover, compared with the waveguide comprised of unbiased graphene (Fig.4-5 (a)) under the same plotting range for the color bar, an increased propagation length can be observed in the lower branch of the biased case, which is due to the dragging effect of drift current in the same direction.

The numerical simulation (COMSOL Multiphysics) set up follows the dispersion curves calculated in the last section, in the left part the upper layer is set with surface conductivity $\sigma_s^{drift}(\omega, q)$ with q equals to -0.063 nm^{-1} and +0.063 nm^{-1} for the lower layer, in agreement with the modes plotted for double graphene layer in Fig.4-4. Whereas for the right part, for the upper branch q is set to an arbitrary negative value, and q = 0.078 nm^{-1} for the lower branch, which is in consistent with the dispersion relation of a single biased graphene layer shown in Fig.4-2. Note that in our configuration adopted here, an approximation is made that the coupling between the two graphene layers when the two layers gradually repels each other is not considered, this is because for the Y-shaped waveguide the two branches in the right part get far

away from each other in a short distance, so we choose to neglect this effect for easy of demonstration here.

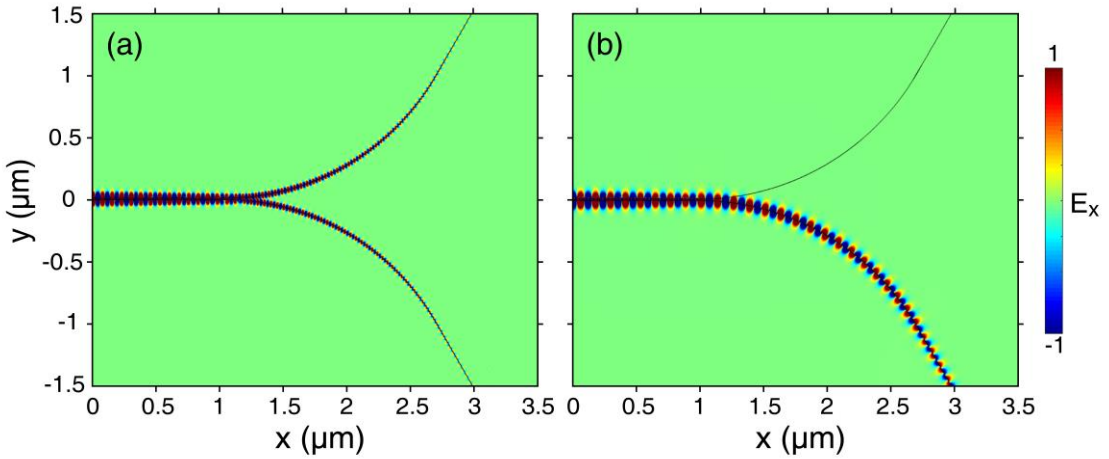

Figure.4-5 Simulated electric field distribution of a Y-shaped waveguide comprised of (a) two unbiased graphene layers and (b) oppositely biased graphene layers at f = 20 THz. The graphene here has relaxation time $\tau = 1$ ps, $\mu_c = 0.1$ eV, T = 300 k. The dipole source is paced at $x_0 = -0.5\ \mu m, z_0 = 10\ nm$ (not shown in the above figures).

Furthermore, as mentioned in Ref. [47], wave instabilities may arise due to the coupling of surface modes of the two graphene layers, which may add interesting functionalities to the waveguide design under study.

4.4 Conclusion

In summary, in this chapter we study the surface plasmon polariton supported by nonreciprocal graphene biased drift electric current. In particular, the unidirectional propagation of SPP over single- and double- layer biased graphene and the corresponding field patterns are analytically studied. At last, we demonstrate a Y-shaped waveguide design with directionality and compare it with the normal unbiased case.

Chapter 5 Summary and outlook

5.1 Summary

This thesis focusses on the coupling and propagation of plasmons in 2D materials, such as graphene monolayer. In particular, the first part (chapter 2) studies the plasmonic interactions between dielectric dimer coated with graphene using a modified transformation-optics (TO) approach. Firstly, the modified TO approach based on conformal mapping is introduced, which is advantageous over traditional analytical approach such as Mie scattering combined with multiple scattering for its computational efficiency, taking advantage of the hidden symmetry of the structure under study. Next, the analytical solution of the spectrum response and field distributions of a graphene-coated nanowire dimer are demonstrated, which features its polarization independent broadband response due to unusual bonding and anti-bonding modes distribution compared to dimer structure without the graphene coating.

The second part of this thesis (chapter 3) studies the broadband all-angle negative refraction of extremely squeezed polaritons in nanostructured and natural anisotropic 2D material. Firstly, the theoretic foundation of this effect, the hyperbolic dispersion of hybrid polaritons supported by anisotropic metasurfaces is derived analytically. Next, two examples of hyperbolic metasurfaces supporting the extremely squeezed polaritons are given, one is based on graphene nanoribbon arrays, another is based on naturally exist anisotropic 2D materials. Our work indicates that 2D materials can serve as a viable platform for novel nanoimaging components, which are of fundamental importance for the active control of light at the nanoscale.

In the third part (chapter 4), the design and verification of a unidirectional waveguide device based on drift induced nonreciprocal graphene plasmon are demonstrated. Firstly, the principle of the drift induced nonreciprocal graphene

plasmon from the respect of the dispersion relations is introduced. Then, the simulation result and detailed analysis of the unidirectional waveguide are given.

5.2 Future work

Finally, for the future work, there are several points that can be improved and further explored on the basis of our current work. Firstly, as mentioned in previous sections, when the surface conductivity of 2D material has a positive imaginary part (i.e. $Im(\sigma_s) > 0$), it acts effectively like a thin metal layer supporting transverse-magnetic (TM) SPPs, and most studies including chapters above are mainly focused on the TM polaritons. Things change when graphene or other 2D materials are nanostructured to become anisotropic [82], chemically doped [40], electrically biased or under mechanical motion [160], where transvers-electric (TE), hybrid TE&TM modes or so-called quasi-TE SPPs may arise. However, TE graphene plasmons are often weakly guided due to their relatively poor spatial confinement [140]. Research shows that stable support of TE modes can be achieved with the aid of a thin hBN slab [161] or high refractive index dielectric and semiconductor materials that have been widely used for waveguide and fiber applications. Therefore, as an extension of our previous work, we may study the exceptional phenomenon associated with TE polaritons, as well as their interplay with TM polaritons in a hybrid system consisting of 2D material such as graphene and hBN or semiconductor materials. In particular, we find that the TE polaritons and TM polaritons excited by a linearly polarized electric dipole source above the metasurface display a 90 degree phase shift, which may be exploited to add extra control of the near field directionality of a Janus or Huygens dipole [162].

Secondly, for the unidirectional waveguide design based on drifted induced graphene plasmon shown in chapter 4, it might be possible to add interesting

functionalities through further investigation of the wave instabilities originate from the interaction of two graphene layers [47] in the left part of the waveguide.

Thirdly, in chapter 2 and chapter 4, nonlocal effects as a result of spatial dispersion may arise when the gap size between two graphene-coated cylinder and the separation between two graphene sheets getting down and the polariton wavelength is squeezed to the level of the Fermi wavelength [31], where nonlocal corrections are needed to refine the theoretic model.

References

[1] A. Otto, Zeitschrift für Physik A Hadrons and nuclei **216**, 398 (1968).
[2] E. Devaux, T. W. Ebbesen, J.-C. Weeber, and A. Dereux, Applied Physics Letters **83**, 4936 (2003).
[3] D. Alcaraz Iranzo *et al.*, Science **360**, 291 (2018).
[4] A. Woessner *et al.*, Nature Materials **14**, 421 (2014).
[5] S. A. Maier, M. L. Brongersma, P. G. Kik, S. Meltzer, A. A. G. Requicha, and H. A. Atwater, Advanced Materials **13**, 1501 (2001).
[6] R. F. Oulton, V. J. Sorger, T. Zentgraf, R.-M. Ma, C. Gladden, L. Dai, G. Bartal, and X. Zhang, Nature **461**, 629 (2009).
[7] C. Haffner *et al.*, Nat Photon **9**, 525 (2015).
[8] A. Emboras, J. Niegemann, P. Ma, C. Haffner, A. Pedersen, M. Luisier, C. Hafner, T. Schimmel, and J. Leuthold, Nano Letters **16**, 709 (2016).
[9] W. L. Barnes, A. Dereux, and T. W. Ebbesen, Nature **424**, 824 (2003).
[10] T. M. Schmidt, PhD Thesis, 2013.
[11] G. Mie, Annalen der physik **330**, 377 (1908).
[12] J. N. Anker, W. P. Hall, O. Lyandres, N. C. Shah, J. Zhao, and R. P. Van Duyne, Nat Mater **7**, 442 (2008).
[13] H. A. Atwater and A. Polman, Nat Mater **9**, 205 (2010).
[14] S. Linic, P. Christopher, and D. B. Ingram, Nature Materials **10**, 911 (2011).
[15] F. Le, D. W. Brandl, Y. A. Urzhumov, H. Wang, J. Kundu, N. J. Halas, J. Aizpurua, and P. Nordlander, ACS Nano **2**, 707 (2008).
[16] A. Kinkhabwala, Z. Yu, S. Fan, Y. Avlasevich, K. Mullen, and W. E. Moerner, Nat Photon **3**, 654 (2009).
[17] C. Argyropoulos, P.-Y. Chen, F. Monticone, G. D'Aguanno, and A. Alù, Physical Review Letters **108**, 263905 (2012).
[18] O. L. Muskens, V. Giannini, J. A. Sánchez-Gil, and J. Gómez Rivas, Nano Letters **7**, 2871 (2007).
[19] A. Delga, J. Feist, J. Bravo-Abad, and F. J. Garcia-Vidal, Physical Review Letters **112**, 253601 (2014).
[20] T. Kokkinakis and K. Alexopoulos, Physical Review Letters **28**, 1632 (1972).
[21] C. Sönnichsen, T. Franzl, T. Wilk, G. von Plessen, J. Feldmann, O. Wilson, and P. Mulvaney, Physical Review Letters **88**, 077402 (2002).
[22] A. Aubry, D. Y. Lei, S. A. Maier, and J. B. Pendry, Physical Review Letters **105**, 233901 (2010).
[23] N. Verellen, Y. Sonnefraud, H. Sobhani, F. Hao, V. V. Moshchalkov, P. V. Dorpe, P. Nordlander, and S. A. Maier, Nano Letters **9**, 1663 (2009).
[24] F. Hao, Y. Sonnefraud, P. V. Dorpe, S. A. Maier, N. J. Halas, and P. Nordlander, Nano Letters **8**, 3983 (2008).
[25] S. Mukherjee, H. Sobhani, J. B. Lassiter, R. Bardhan, P. Nordlander, and N. J. Halas, Nano Letters **10**, 2694 (2010).
[26] U. Fano, Physical Review **124**, 1866 (1961).
[27] J. A. Fan *et al.*, Science **328**, 1135 (2010).
[28] A. Kinkhabwala, Z. Yu, S. Fan, Y. Avlasevich, K. Müllen, and W. E. Moerner, Nature Photonics **3**, 654 (2009).
[29] L. Vicarelli, M. S. Vitiello, D. Coquillat, A. Lombardo, A. C. Ferrari, W. Knap, M. Polini, V. Pellegrini, and A. Tredicucci, Nature Materials **11**, 865 (2012).

[30] D. Rodrigo, O. Limaj, D. Janner, D. Etezadi, F. J. García de Abajo, V. Pruneri, and H. Altug, Science **349**, 165 (2015).
[31] D. N. Basov, M. M. Fogler, and F. J. García de Abajo, Science **354** (2016).
[32] K. I. Bolotin, K. J. Sikes, Z. Jiang, M. Klima, G. Fudenberg, J. Hone, P. Kim, and H. L. Stormer, Solid State Communications **146**, 351 (2008).
[33] T. Low *et al.*, Nature Materials **16**, 182 (2016).
[34] T. Low and P. Avouris, ACS Nano **8**, 1086 (2014).
[35] F. H. L. Koppens, D. E. Chang, and F. J. García de Abajo, Nano Letters **11**, 3370 (2011).
[36] L. Ju *et al.*, Nature Nanotechnology **6**, 630 (2011).
[37] H. Yan, T. Low, W. Zhu, Y. Wu, M. Freitag, X. Li, F. Guinea, P. Avouris, and F. Xia, Nature Photonics **7**, 394 (2013).
[38] G. X. Ni *et al.*, Nature Photonics **10**, 244 (2016).
[39] V. P. Gusynin, S. G. Sharapov, and J. P. Carbotte, Journal of Physics: Condensed Matter **19**, 026222 (2007).
[40] A. Vakil and N. Engheta, Science **332**, 1291 (2011).
[41] R. R. Nair, P. Blake, A. N. Grigorenko, K. S. Novoselov, T. J. Booth, T. Stauber, N. M. R. Peres, and A. K. Geim, Science **320**, 1308 (2008).
[42] Z. Fei *et al.*, Nature **487**, 82 (2012).
[43] J. Chen *et al.*, Nature **487**, 77 (2012).
[44] S. Bae *et al.*, Nature Nanotechnology **5**, 574 (2010).
[45] Y. Liu, R. Cheng, L. Liao, H. Zhou, J. Bai, G. Liu, L. Liu, Y. Huang, and X. Duan, Nature Communications **2**, 579 (2011).
[46] M. Liu, X. Yin, E. Ulin-Avila, B. Geng, T. Zentgraf, L. Ju, F. Wang, and X. Zhang, Nature **474**, 64 (2011).
[47] T. A. Morgado and M. G. Silveirinha, Physical Review Letters **119**, 133901 (2017).
[48] S. Thongrattanasiri, F. H. L. Koppens, and F. J. García de Abajo, Physical Review Letters **108**, 047401 (2012).
[49] P.-Y. Chen and A. Alù, ACS Nano **5**, 5855 (2011).
[50] R. Li, X. Lin, S. Lin, X. Zhang, E. Li, and H. Chen, Carbon **98**, 463 (2016).
[51] R. J. Li, X. Lin, S. S. Lin, X. Liu, and H. S. Chen, Opt. Lett. **40**, 1651 (2015).
[52] T. Christensen, A.-P. Jauho, M. Wubs, and N. A. Mortensen, Physical Review B **91**, 125414 (2015).
[53] D. A. Smirnova, I. V. Shadrivov, A. E. Miroshnichenko, A. I. Smirnov, and Y. S. Kivshar, Physical Review B **90**, 035412 (2014).
[54] F. Schedin, E. Lidorikis, A. Lombardo, V. G. Kravets, A. K. Geim, A. N. Grigorenko, K. S. Novoselov, and A. C. Ferrari, ACS Nano **4**, 5617 (2010).
[55] Z. Fang, Y. Wang, Z. Liu, A. Schlather, P. M. Ajayan, F. H. L. Koppens, P. Nordlander, and N. J. Halas, ACS Nano **6**, 10222 (2012).
[56] X. Lin *et al.*, Proceedings of the National Academy of Sciences **114**, 6717 (2017).
[57] T. Mueller, F. Xia, and P. Avouris, Nature Photonics **4**, 297 (2010).
[58] F. Xia, H. Wang, D. Xiao, M. Dubey, and A. Ramasubramaniam, Nature Photonics **8**, 899 (2014).
[59] K. F. Mak, K. He, J. Shan, and T. F. Heinz, Nature Nanotechnology **7**, 494 (2012).
[60] X. Huang *et al.*, ACS Photonics (2018).
[61] X. Wang *et al.*, Nature Nanotechnology **10**, 517 (2015).

[62] A. Nemilentsau, T. Low, and G. Hanson, Physical Review Letters **116**, 066804 (2016).
[63] S. Dai *et al.*, Nature Communications **6**, 6963 (2015).
[64] R. A. Shelby, D. R. Smith, and S. Schultz, Science **292**, 77 (2001).
[65] B. Edwards, A. Alù, M. E. Young, M. Silveirinha, and N. Engheta, Physical Review Letters **100**, 033903 (2008).
[66] R. Liu, Q. Cheng, T. Hand, J. J. Mock, T. J. Cui, S. A. Cummer, and D. R. Smith, Physical Review Letters **100**, 023903 (2008).
[67] J. B. Pendry, D. Schurig, and D. R. Smith, Science **312**, 1780 (2006).
[68] U. Leonhardt, Science **312**, 1777 (2006).
[69] D. Schurig, J. J. Mock, B. J. Justice, S. A. Cummer, J. B. Pendry, A. F. Starr, and D. R. Smith, Science **314**, 977 (2006).
[70] M. Rahm, S. A. Cummer, D. Schurig, J. B. Pendry, and D. R. Smith, Physical Review Letters **100**, 063903 (2008).
[71] H. Chen, B. Hou, S. Chen, X. Ao, W. Wen, and C. T. Chan, Physical Review Letters **102**, 183903 (2009).
[72] G. Zheng, H. Mühlenbernd, M. Kenney, G. Li, T. Zentgraf, and S. Zhang, Nature Nanotechnology **10**, 308 (2015).
[73] J. Lin, J. P. B. Mueller, Q. Wang, G. Yuan, N. Antoniou, X.-C. Yuan, and F. Capasso, Science **340**, 331 (2013).
[74] G. V. Viktor, Soviet Physics Uspekhi **10**, 509 (1968).
[75] J. B. Pendry, Physical Review Letters **85**, 3966 (2000).
[76] N. Fang, H. Lee, C. Sun, and X. Zhang, Science **308**, 534 (2005).
[77] N. Yu and F. Capasso, Nature Materials **13**, 139 (2014).
[78] X. Yin, Z. Ye, J. Rho, Y. Wang, and X. Zhang, Science **339**, 1405 (2013).
[79] P. Li *et al.*, Science **359**, 892 (2018).
[80] E. Forati, G. W. Hanson, A. B. Yakovlev, and A. Alù, Physical Review B **89**, 081410 (2014).
[81] Z. Jacob and E. E. Narimanov, Applied Physics Letters **93**, 221109 (2008).
[82] J. S. Gomez-Diaz, M. Tymchenko, and A. Alù, Physical Review Letters **114**, 233901 (2015).
[83] E. Prodan, C. Radloff, N. J. Halas, and P. Nordlander, Science **302**, 419 (2003).
[84] A. Aubry, D. Y. Lei, S. A. Maier, and J. B. Pendry, ACS Nano **5**, 3293 (2011).
[85] D. Y. Lei, A. Aubry, Y. Luo, S. A. Maier, and J. B. Pendry, ACS Nano **5**, 597 (2011).
[86] A. Aubry, D. Y. Lei, S. A. Maier, and J. B. Pendry, Physical Review B **82**, 125430 (2010).
[87] J. B. Pendry, A. Aubry, D. R. Smith, and S. A. Maier, Science **337**, 549 (2012).
[88] M. Kraft, J. B. Pendry, S. A. Maier, and Y. Luo, Physical Review B **89**, 245125 (2014).
[89] J. B. Pendry, A. I. Fernandez-Dominguez, Y. Luo, and R. Zhao, Nat Phys **9**, 518 (2013).
[90] A. Aubry, D. Y. Lei, A. I. Fernández-Domínguez, Y. Sonnefraud, S. A. Maier, and J. B. Pendry, Nano Letters **10**, 2574 (2010).
[91] Y. Luo, D. Y. Lei, S. A. Maier, and J. B. Pendry, Physical Review Letters **108**, 023901 (2012).
[92] Y. Luo, D. Y. Lei, S. A. Maier, and J. B. Pendry, ACS Nano **6**, 6492 (2012).
[93] A. Aubry, D. Y. Lei, S. A. Maier, and J. B. Pendry, Physical Review B **82**, 205109 (2010).

[94] A. I. Fernández-Domínguez, A. Wiener, F. J. García-Vidal, S. A. Maier, and J. B. Pendry, Physical Review Letters **108**, 106802 (2012).
[95] Y. Luo, A. I. Fernandez-Dominguez, A. Wiener, S. A. Maier, and J. B. Pendry, Physical Review Letters **111**, 093901 (2013).
[96] P. A. Huidobro, M. Kraft, R. Kun, S. A. Maier, and J. B. Pendry, Journal of Optics **18**, 044024 (2016).
[97] A. N. Grigorenko, M. Polini, and K. S. Novoselov, Nature Photonics **6**, 749 (2012).
[98] L. Ju *et al.*, Nat Nano **6**, 630 (2011).
[99] T. Christensen, W. Yan, A.-P. Jauho, M. Wubs, and N. A. Mortensen, Physical Review B **92**, 121407 (2015).
[100] Y. Gao and I. V. Shadrivov, Opt. Lett. **41**, 3623 (2016).
[101] A. I. Fernández-Domínguez, S. A. Maier, and J. B. Pendry, Physical Review Letters **105**, 266807 (2010).
[102] M. Kraft, Y. Luo, S. A. Maier, and J. B. Pendry, Physical Review X **5**, 031029 (2015).
[103] S. M. Hanham *et al.*, Advanced Materials **24**, OP226 (2012).
[104] J. A. Kong, *Electromagnetic Wave Theory* (Wiley, 1986).
[105] J. Jiang, D. Zhang, B. Zhang, and Y. Luo, Opt. Lett. **42**, 2890 (2017).
[106] J. B. Pendry and S. A. Ramakrishna, Journal of Physics: Condensed Matter **14**, 8463 (2002).
[107] R. Schinzinger and P. A. Laura, *Conformal mapping: methods and applications* (Courier Corporation, 2003).
[108] H.-T. Chen, H. Lu, A. K. Azad, R. D. Averitt, A. C. Gossard, S. A. Trugman, J. F. O'Hara, and A. J. Taylor, Opt. Express **16**, 7641 (2008).
[109] E. Hendry, F. J. Garcia-Vidal, L. Martin-Moreno, J. G. Rivas, M. Bonn, A. P. Hibbins, and M. J. Lockyear, Physical Review Letters **100**, 123901 (2008).
[110] V. Giannini, A. Berrier, S. A. Maier, J. A. Sánchez-Gil, and J. G. Rivas, Opt. Express **18**, 2797 (2010).
[111] P.-Y. Chen, J. Soric, and A. Alù, Advanced Materials **24**, OP281 (2012).
[112] S. Liu, H. C. Zhang, H.-X. Xu, and T. J. Cui, J. Opt. Soc. Am. A **31**, 2075 (2014).
[113] S. Thongrattanasiri and F. J. García de Abajo, Physical Review Letters **110**, 187401 (2013).
[114] X. Lin *et al.*, Science Advances **3** (2017).
[115] L. J. Wong, I. Kaminer, O. Ilic, J. D. Joannopoulos, and M. Soljačić, Nature Photonics **10**, 46 (2015).
[116] G. X. Ni *et al.*, Nature **557**, 530 (2018).
[117] X. Shi, X. Lin, I. Kaminer, F. Gao, Z. Yang, J. D. Joannopoulos, M. Soljačić, and B. Zhang, arXiv preprint arXiv:1805.12427 (2018).
[118] E. Yoxall *et al.*, Nature Photonics **9**, 674 (2015).
[119] S. Chakraborty, O. P. Marshall, T. G. Folland, Y.-J. Kim, A. N. Grigorenko, and K. S. Novoselov, Science **351**, 246 (2016).
[120] S. Dai *et al.*, Science **343**, 1125 (2014).
[121] P. Li, M. Lewin, A. V. Kretinin, J. D. Caldwell, K. S. Novoselov, T. Taniguchi, K. Watanabe, F. Gaussmann, and T. Taubner, Nature Communications **6**, 7507 (2015).
[122] C. Qian *et al.*, ACS Photonics **5**, 1506 (2018).
[123] J. Yuyu, L. Xiao, L. Tony, Z. Baile, and C. Hongsheng, Laser & Photonics Reviews **12**, 1800049 (2018).

[124] L. J. J. *et al.*, Small **14**, 1800072 (2018).
[125] A. A. High, R. C. Devlin, A. Dibos, M. Polking, D. S. Wild, J. Perczel, N. P. de Leon, M. D. Lukin, and H. Park, Nature **522**, 192 (2015).
[126] J. S. T. Smalley *et al.*, Nature Communications **8**, 13793 (2017).
[127] Y. Yang *et al.*, Npg Asia Materials **9**, e428 (2017).
[128] A. Poddubny, I. Iorsh, P. Belov, and Y. Kivshar, Nature Photonics **7**, 948 (2013).
[129] V. V. Cheianov, V. Fal'ko, and B. L. Altshuler, Science **315**, 1252 (2007).
[130] G.-H. Lee, G.-H. Park, and H.-J. Lee, Nature Physics **11**, 925 (2015).
[131] S. Chen *et al.*, Science **353**, 1522 (2016).
[132] H. Harutyunyan, R. Beams, and L. Novotny, Nature Physics **9**, 423 (2013).
[133] B. Wang, X. Zhang, F. J. García-Vidal, X. Yuan, and J. Teng, Physical Review Letters **109**, 073901 (2012).
[134] H. Huang, B. Wang, H. Long, K. Wang, and P. Lu, Opt. Lett. **39**, 5957 (2014).
[135] K. V. Sreekanth, A. D. Luca, and G. Strangi, Applied Physics Letters **103**, 023107 (2013).
[136] A. A. Sayem, M. M. Rahman, M. R. C. Mahdy, I. Jahangir, and M. S. Rahman, Scientific Reports **6**, 25442 (2016).
[137] S. Zhong, Y. Lu, C. Li, H. Xu, F. Shi, and Y. Chen, Scientific Reports **7**, 41788 (2017).
[138] M. Jablan, H. Buljan, and M. Soljačić, Physical Review B **80**, 245435 (2009).
[139] L. Xiao, R. Nicholas, J. L. Josué, K. Ido, C. Hongsheng, and S. Marin, New Journal of Physics **18**, 105007 (2016).
[140] S. A. Mikhailov and K. Ziegler, Physical Review Letters **99**, 016803 (2007).
[141] G. Fernando and V. Y. Oleg, 2D Materials **5**, 015019 (2018).
[142] X. Lin, Y. Shen, I. Kaminer, H. Chen, and M. Soljačić, Physical Review A **94**, 023836 (2016).
[143] I. J. O. *et al.*, Advanced Optical Materials **2**, 641 (2014).
[144] D. Jun and Z. X. Cheng, Angewandte Chemie **127**, 7682 (2015).
[145] J. Kang, H. Sahin, H. D. Ozaydin, R. T. Senger, and F. M. Peeters, Physical Review B **92**, 075413 (2015).
[146] G. W. Hanson, IEEE Transactions on Antennas and Propagation **56**, 747 (2008).
[147] H. Shin and S. Fan, Physical Review Letters **96**, 073907 (2006).
[148] H. J. Lezec, J. A. Dionne, and H. A. Atwater, Science **316**, 430 (2007).
[149] A. Y. Nikitin *et al.*, Nature Photonics **10**, 239 (2016).
[150] Z. Wang, Y. Chong, J. D. Joannopoulos, and M. Soljačić, Nature **461**, 772 (2009).
[151] X. Lin, Y. Xu, B. Zhang, R. Hao, H. Chen, and E. Li, New Journal of Physics **15**, 113003 (2013).
[152] B. Zhu, G. Ren, Y. Gao, B. Wu, Q. Wang, C. Wan, and S. Jian, Optics Express **23**, 16071 (2015).
[153] D. Correas-Serrano, A. Alù, and J. S. Gomez-Diaz, Physical Review B **98**, 165428 (2018).
[154] D. L. Sounas, J. Soric, and A. Alù, Nature Electronics **1**, 113 (2018).
[155] T. A. Morgado and M. G. Silveirinha, ACS Photonics **5**, 4253 (2018).
[156] V. E. Dorgan, A. Behnam, H. J. Conley, K. I. Bolotin, and E. Pop, Nano Letters **13**, 4581 (2013).
[157] M. A. Yamoah, W. Yang, E. Pop, and D. Goldhaber-Gordon, ACS Nano **11**, 9914 (2017).
[158] H. Ramamoorthy, R. Somphonsane, J. Radice, G. He, C. P. Kwan, and J. P. Bird, Nano Letters **16**, 399 (2016).

[159] G. W. Hanson, S. A. Hassani Gangaraj, C. Lee, D. G. Angelakis, and M. Tame, Physical Review A **92**, 013828 (2015).
[160] Y. Mazor and A. Alù, arXiv preprint arXiv:1809.01638 (2018).
[161] M. Musa, M. Renuka, X. Lin, R. Li, H.Wang, E. Li, B. Zhang, and H. Chen, 2D Materials **5**, 015018 (2018).
[162] M. F. Picardi, A. V. Zayats, and F. J. Rodríguez-Fortuño, Physical Review Letters **120**, 117402 (2018).

Publication

Jing Jiang, Daohua Zhang, Baile Zhang, Yu Luo, Interaction between graphene-coated nanowires revisited with transformation optics, *Optics Letters*, 42(15) (2017) 2890-2893.

Guangcan Li, Yongliang Zhang, Jing Jiang, Yu Luo, Dangyuan Lei, Metal-Substrate-Mediated Plasmon Hybridization in a Nanoparticle Dimer for Photoluminescence Line-Width Shrinking and Intensity Enhancement, *ACS Nano*, 11(3) (2017) 3067-3080.

Jing Jiang, Xiao Lin, Baile Zhang, Broadband all-angle negative refraction of highly squeezed graphene plasmons, *Research*, 2018 (2018) 2532819.